KVIK Optimiser - An Enhanced ReaxFF Force Field Training Approach

Daniel Gaissmaier,[†,‡,¶] Matthias van den Borg,[†] Donato Fantauzzi,[§] and Timo Jacob[*,†,‡,¶]

†*Institute of Electrochemistry, Ulm University, Albert-Einstein-Allee 47, D-89081 Ulm, Germany*

‡*Helmholtz-Institute Ulm (HIU) for Electrochemical Energy Storage, Helmholtzstr. 11, 89081 Ulm, Germany*

¶*Karlsruhe Institute of Technology (KIT), P.O. Box 3640, 76021 Karlsruhe, Germany*

§*Faculty of Physical Sciences, University of Iceland VR-III, 107 Reykjavik, Iceland*

E-mail: timo.jacob@uni-ulm.de

Abstract

In this work, we demonstrate the superior exploration capabilities of the population-based methods over the sequential one-parameter parabolic interpolation (SOPPI) approach to optimise ReaxFF force field parameters. Evolutionary algorithms (EAs) are heuristic-based approaches using a population of concurrent models in the search space to evolve towards the global best through stochastic operations. The parallelisation of EAs scales almost linearly, and no differentiable objective function is required. These methods were tested for their search performance and convergence behaviour on different multi-dimensional, multimodal benchmark functions. The developed *KVIK* (*Icelandic for: dynamic, in motion*) optimisation framework features an extended training

routine designed to parameterise solid-state systems efficiently. The optimisation routine was applied to train a reactive force field potential for metallic lithium and sodium and their interaction parameters. The KVIK-optimised ReaxFF potential function parameter set reproduces relative energy results from the density functional theory (DFT) reference data set within the standard deviation range established using the error estimation routine provided by the BEEF-vdW density functional. Finally, thermodynamically and kinetically driven surface growth phenomena on metallic Li- and Na-electrodes were investigated using coupled ReaxFF/Monte Carlo (MC) approaches.

1 Introduction

Quantum mechanical methods such as Hartree-Fock (HF), configuration interaction (CI), coupled cluster (CC) or density functional theory (DFT) are powerful tools to study the electronic properties of molecular structures or solid-state systems. However, due to their high computational cost, these methods are still limited to short simulation times and small systems with a few hundred atoms. The bond order based reactive force field (ReaxFF)[1–4] approach overcomes these limitations and enables large scale (up to 100.000 atoms) and long-term (several nanoseconds) fully reactive simulations for complex systems. The accuracy of the force field potential depends heavily on the scope and quality of the chosen training and validation set. Within the force field development process, many physical and empirical parameters (in some cases hundreds) have to be fitted to higher-level theoretical or experimental reference data. Pre-existing correlations between the parameters and discontinuities in the error function further aggravate the optimisation task.[5] Identifying the local optima of this multimodal optimisation problem is a substantial challenge and, in most cases, only feasible with a deep chemical understanding of the underlying formalism.

The sequential one-parameter parabolic interpolation (SOPPI) method has been used as one of the first techniques for the development of ReaxFF force fields.[6] Here, the total error is calculated for three different values of a selected parameter to derive the optimal value

using a parabolic fit. However, with an increasing set of parameters, the required number of one-parameter optimisation steps to achieve overall convergence increases dramatically, as only a small portion of the search space is accessible. Also, it requires a reasonable initial guess and a well-considered choice of the order for the parameters to be optimised in each step to obtain an accurate solution.[7]

In recent years, different non-deterministic global optimisation strategies such as Monte Carlo methods,[8–10] genetic algorithms,[5,11–14] stochastic optimisation techniques[10,15,16] or machine learning-based approaches[14,17–20] have been adopted to enhance the optimisation performance.

An important class of global optimisation methods are evolutionary algorithms (EAs), which are inspired by the natural evolution of species and show excellent convergence rates. Here, a population of concurrent models are used, which evolve towards better models by stochastic processes. The simultaneous evaluation of the independent models enables a high level of parallelisation for these algorithms resulting in a significant reduction in computing time. The particle swarm optimisation (PSO) belongs to the class of evolutionary algorithms and was introduced by Kennedy and Eberhart in 1995.[21] This approach mimics the behaviour of bird flocks and fish schooling to guide the particles in finding the global optimal solutions in complex multi-dimensional model parameter spaces.

The differential evolution (DE) algorithm is a population-based algorithm introduced by Storn and Price in 1997.[22] This EA uses mutation as a search mechanism and uses the selection operation to direct the search of the potential regions of the model parameter space. Both algorithms do not require a differentiable optimisation problem and are characterised by their robustness, simplicity, strong ability to find globally optimal solutions for highly nonlinear and nonconvex problems, and the small number of necessary tuning parameters.[23,24] In this way, these methods come to be ideal candidates to be used for the parametrisation of ReaxFF potentials.

This work is divided into two parts: In the first part, we propose a new procedure for optimis-

ing reactive force fields using evolutionary algorithms. The different algorithms are tested and evaluated on representative benchmark functions. Further, we extended the classical training by important solid-state properties such as bulk moduli, vibrational frequencies, or diffusion barriers to better describe the system's surface properties.

The second part applies the *KVIK* optimisation routine to parametrise a reactive force field for metallic electrode materials. Here, a significant challenge arises in accurately reproducing the subtle energy differences between the diffusion processes. Our parameterised ReaxFF potential function for Li-Li, Na-Na, and Li-Na interactions demonstrate an excellent agreement with *ab initio* based DFT calculations. It must be emphasised that even the subtle energy differences are reproduced accurately, which constitutes a significant challenge for these systems. Finally, the generated force field is used for grand canonical and kinetic Monte Carlo simulations to study the initial growth phenomena on metallic electrode materials. First, thermodynamically controlled growth phenomena on Li and Na nanoparticles were investigated using a ReaxFF/grand canonical Monte Carlo (GCMC) approach. Then, the influence of kinetics on the surface growth of Li(100) and Na(100) was studied within the framework of kinetic Monte Carlo (kMC) simulations.

Part I: Development and implementation of the KVIK approach

2 Theoretical background

2.1 Evolutionary algorithms

Evolutionary algorithms are inspired by natural groups or swarm behaviour of animals and feature excellent convergence rates. These algorithms utilise a population of competing models that evolve into better models through stochastic processes.

In this work, we tested and validated different optimisation routines, namely particle swarm optimisation (PSO),[21] competitive particle swarm optimisation (CPSO),[25] differential evolution (DE),[22,26] covariance matrix adaptation - evolution strategy (CMA-ES),[27–29] and linear variant of covariance matrix adaptation (VD-CMA).[30] An overview of the algorithms used for the force field optimisation is given below.

2.1.1 Particle Swarm Optimisation

Kennedy and Eberhart introduced the particle swarm optimisation routine in 1995, which mimics the behaviour of bird flocks and fish schooling.[21] The underlying optimisation routine can be described in terms of three simple behavioural patterns:[31]

(i) Separation – Avoiding crowded local flockmates

(ii) Alignment – Moving towards the average direction of the local flockmates

(iii) Cohesion – Moving towards the average position of local flockmates

This swarm intelligence-based EA is characterised by its robustness, simplicity and fast convergence rate.

At the beginning of the optimisation, a swarm of multiple particles is generated in the model parameter space. The initial particle positions can be defined *a priori* or be determined by a (uniform) random distribution. Next, the fitness values of the individual particles are computed before updating the individual and global best values. Finally, the velocities $\mathbf{v}$ and positions $\mathbf{x}$ of the respective particles will be updated as follows:

$$\mathbf{v}_i^k = \omega \mathbf{v}_i^{k-1} + \phi_\mathrm{p} \mathbf{r}_\mathrm{p}^k \left(\mathbf{x}_{\mathrm{p},i} - \mathbf{x}_i^{k-1} \right) + \phi_\mathrm{g} \mathbf{r}_\mathrm{g}^k \left(\mathbf{x}_\mathrm{g} - \mathbf{x}_i^{k-1} \right) \tag{1}$$

$$\mathbf{x}_i^k = \mathbf{x}_i^{k-1} + \mathbf{v}_i^k \tag{2}$$

where $\mathbf{v}_i^k$ is the velocity vector of particle i at iteration k, ω is an inertia weight, $\mathbf{x}_{\mathrm{p},i}$ is the personal best position of the particle i, $\mathbf{x}_g$ is the global best position of the swarm, $\mathbf{r}_\mathrm{p}^k$ and $\mathbf{r}_\mathrm{g}^k$ are uniform random number vectors, ϕ_p and ϕ_g are acceleration parameters, respectively. The inertial weighting was not included in the original formulation of the velocity equation and was first introduced by Shi and Eberhart in 1998.[32,33] Their form of Eq. (1) later became accepted as the new 'standard' for the PSO. Due to the resulting dynamic adjustment of the particle velocities, it refines the search in the direct vicinity of the minimum. Thus, an optimisation of the convergence speed as well as an enhancement of the final solution is achieved.

In the first part of the velocity update formula (Eq. (1)), the particle's previous velocity is taken into account. Here, the particle performs an inertial motion depending on its own velocity and the inertial weight parameter ω. The second part is related to the distance between the particle's personal best position $\mathbf{x}_{\mathrm{p},i}$ and its current location $\mathbf{x}_i^{k-1}$. This "cognitive" element represents the particle's own thinking based on its individual experience and is controlled by the cognitive acceleration factor ϕ_p (or cognitive learning factor). The third part forms the "social" element and depends on the distance between the global best position $\mathbf{x}_\mathrm{g}$ and the current particle location $\mathbf{x}_i^{k-1}$. Each particle's movement is affected by the previous experience of the swarm. In this way, knowledge transfer and cooperation between the respective swarm members emerge. The impact of the collective can be controlled via the social acceleration factor ϕ_g (or social learning factor).[34]

The overall performance of the PSO can be controlled by the chosen control parameters. Based on Clerc's constriction method,[35] Eberhart and Shi identified $\omega = 0.7298$ and $\phi_\mathrm{p} = \phi_\mathrm{g} = 1.49618$ as a reliable set of parameters to obtain well-converged solutions.[33] The choice of the swarm size and the maximum number of iterations depends strongly on the complexity of the optimisation problem and the available computing resources. In general, a larger population size increases the success rate but raises the number of misfit function evaluations.[25] PSOs can be numerically implemented as synchronous or asynchronous algorithms. While

in the synchronous case, the global best is determined after the end of each iteration, $\mathbf{x}_\mathrm{g}$ is updated after each misfit evaluation in the asynchronous setup. Asynchronous optimisation increases the diversity of the swarm, whereas synchronous PSO includes more information from the previous iteration.[36–38] Various studies showed superior performance of the asynchronous PSO;[36,39–41] however, the increased need for communication complicates the parallelisation of the algorithm considerably.[42,43]

2.1.2 Competitive Particle Swarm Optimisation

The traditional PSO is characterised by its robustness, simplicity and the small number of required tuning parameters. However, premature convergence and stagnation at a local extreme are more likely to occur for more complex model parameter spaces.[25,34] To address this issue, Luu *et al.*[25] have developed the CPSO. Here, the traditional PSO algorithm is used, but the diversity of the swarm is increased by resetting the "worst" particles. While the preserved "best" particles are sampling for the minimum in the vicinity of the current best position, the newly generated particles are exploring the model parameter space for a potential better minimum. Once a better minimum is found, the swarm will be assembled around the new global best value. Resetting part of the population is called "competition" and will only be initiated when a premature convergence of the optimisation is found. Here the maximum radius of the swarm δ^k at iteration k determines the premature convergence and is defined as:

$$\delta^k = \max_{1 \leq i \leq s} \left(\frac{\|\mathbf{x}_i^k - \mathbf{x}_g\|}{\|\mathbf{x}_\mathrm{max} - \mathbf{x}_\mathrm{min}\|} \right) \tag{3}$$

A "competition" is triggered when the swarm's maximum radius δ^k is smaller than the user-defined threshold ε:

$$\delta^k < \varepsilon = \frac{\log\left(1 + 0.003s\right)}{\max\left(0.2, \log\left[0.01 k_\mathrm{max}\right]\right)}. \tag{4}$$

The expression for the threshold ε is purely empirical and depends on the swarm size s and the maximum number of iterations $k_{\max}$. In order to determine the fraction of particles to reset at a given iteration k, a logistic function $\sigma(k)$ is introduced as

$$\sigma(k) = \frac{1}{1 + \exp\left(\frac{1}{0.09}\left[\frac{k}{k_{\max}} - \gamma + 0.5\right]\right)}, \quad \gamma \in [0, 2]\,. \tag{5}$$

In this way, the proportion of particles to reset decreases with the number of iterations and thus maintain the convergence property of a PSO. The introduced competitivity parameter γ can control the position of the inflexion point. In general, the choice of the competitivity parameter depends on the optimisation problem, although $\gamma = 1$ has proven to be a reasonable initial guess in most cases. For $\gamma = 0$, the classical PSO behaviour is preserved, as no particles are reset at any iteration.

Compared to the classical PSO, the CPSO provides a better convergence rate, improved sampling of the model parameter space and thus offers a robust uncertainty quantification.[25]

2.1.3 Differential Evolution

The DE algorithm is a population-based optimisation method introduced by Storn and Price in 1997.[22] The optimisation procedure can be divided into three parts, namely mutation, crossover, and selection.[24,44]

For the investigation of the model parameter space, N_{P} D-dimensional parameter vectors for each generation G are used:

$$\mathbf{x}_{i,G}, \quad i = 1, .., N_{\mathrm{P}} \tag{6}$$

Also, three types of parameter vectors are required for the DE algorithm: target vector, mutation vector and trail vector. At the beginning of the optimisation, the parameter vectors within the model parameter space, which holds the possible solution candidates, are initiated. The initial population is generated by a uniform random distribution of individuals in the

model parameter space or built from a preliminary solution with added random deviations.[22] The current solution of the optimisation problem becomes the target vector.

In the mutation step, a mutation vector $\mathbf{v}_{i,G+1}$ is generated[1] for each of the N_P target vectors $\mathbf{x}_{i,G}$ following

$$\mathbf{v}_{i,G+1} = \mathbf{x}_{r_1,G} + F\left(\mathbf{x}_{r_2,G} - \mathbf{x}_{r_3,G}\right), \quad F \in [0,2],\ r_1, r_2, r_3 \in \{1,..,N_\mathrm{P}\}\ , \tag{7}$$

where r_1, r_2, r_3 are random indices and F is a scaling factor for the differential variation. Next, a crossover operation is done to increase the diversity of the perturbed parameter vectors. Thus, a trail vector $\mathbf{u}_{i,G+1}$ is constructed by mixing the mutation vector $\mathbf{v}_{i,G+1}$ and the target vector $\mathbf{x}_{i,G}$[46] following

$$\mathbf{u}_{i,G+1} = (\mathbf{u}_{1i,G+1}, \mathbf{u}_{2i,G+1}, .., \mathbf{u}_{Di,G+1}) \tag{8}$$

$$\mathbf{u}_{ji,G+1} = \begin{cases} \mathbf{v}_{ji,G+1} & \text{if } R_j \leq CR \\ \mathbf{x}_{ji,G} & \text{if } R_j > CR \end{cases}, \quad j = 1,..,D \tag{9}$$

where R_j is a uniform random real number between [0,1], and CR is the crossover constant ($CR \in [0,1]$).

In the selection step, the fitness values of the trail vector $u_{i,G+1}$ and the target vector $x_{i,G}$ are compared. If the trail vector has a smaller cost function, $u_{i,G+1}$ will be defined as the new target vector $x_{i,G+1}$ of generation $G+1$; otherwise, the old target vector will be retained.

The steps mutation, crossover, and selection are executed successively in an iterative manner until the respective termination criterion is reached.

[1] Different strategies have been developed for generating the mutation vector.[45] In Eq. (7), the formulation of Storn and Price[22] (*rand1bin* strategy) is given. Further strategies are summarised in Appendix C.4.

2.2 Transition state tools

Identifying the minimum energy path (MEP) and the associated transition state is essential for investigating reaction mechanisms and diffusion properties. For the parametrisation of reactive force fields, these findings are vital data for the training and validation of the potential for an accurate description of the reaction kinetics and the potential energy landscape. Based on the Transition State tools for VASP (VTST) by Henkelman and Jónsson,[47] we have implemented various methods and tools to explore the MEP of the system within the ReaxFF application of the Amsterdam Modeling Suite.[48]

(i) nudged elastic band (NEB) method:[49–52]

- climbing image nudged elastic band (CI-NEB) method[49]
- Nudged Elastic Band method with the removal of translational and rotational degrees of freedom (NEB-TR)[52]

(ii) Dimer method,[53–55] Lanczos method[56,57]

(iii) Force-based optimisers with constraints:

- Fast inertial relaxation engine (FIRE)[51,58]
- Polak-Ribière conjugate gradient (CG)[51,59,60]
- Limited-memory Broyen-Fletcher-Goldfarb-Shanno (L-BFGS)[51,61]
- Steepest descents (SD)[51]
- Quick-Min (QM)[51]

(iv) Vibration analysis[62,63]

The implementation is available as of Amsterdam Modeling Suite 2018 and later.[48] Instructions on how to use the transition state tools within the ReaxFF implementation are given in Appendix A.

In the following, we summarise the theoretical background for the applied methods within the scope of this work. Additional information can be found in the listed literature.

2.2.1 Climbing Image Nudged Elastic Band Method

The CI-NEB approach is a chain-of-states based method designed to locate the MEP between two stable system states on a potential energy landscape.[49,50] Here, an elastic band consisting of $N+1$ images describes the reaction pathway, keeping the initial and final states fixed. The respective system configurations $[\mathbf{R}_0, \mathbf{R}_1, ..., \mathbf{R}_N]$ are separated by a spring constant to guarantee the continuity of the pathway. In order to find the MEP, the $N-1$ intermediate images are adjusted by a force-based optimisation algorithm. The total force $\mathbf{F}_i^{\mathrm{NEB}}$ acting on the image i is defined through a force projection scheme consisting of the potential forces acting perpendicular to the band $\mathbf{F}_i^{\perp}$ and the spring forces along the band $\mathbf{F}_i^{\mathrm{S}\parallel}$, following

$$\mathbf{F}_i^{\mathrm{NEB}} = \mathbf{F}_i^{\perp} + \mathbf{F}_i^{S\parallel} \tag{10}$$

with

$$\mathbf{F}_i^{\perp} = -\nabla V(\mathbf{R}_i) + \nabla V(\mathbf{R}_i)\hat{\boldsymbol{\tau}}_i\hat{\boldsymbol{\tau}}_i \tag{11}$$

$$\mathbf{F}_i^{\mathrm{S}\parallel} = k\left(|\mathbf{R}_{i+1} - \mathbf{R}_i| - |\mathbf{R}_i - \mathbf{R}_{i-1}|\right)\hat{\boldsymbol{\tau}}_i\,. \tag{12}$$

where k is a spring constant, and $\hat{\boldsymbol{\tau}}_i = \boldsymbol{\tau}_i / |\boldsymbol{\tau}_i|$ a normalised up-winding tangent. Depending on the potential energy V of the adjacent images, the tangent is defined by

$$\boldsymbol{\tau}_i = \begin{cases} \mathbf{R}_{i+1} - \mathbf{R}_i & \text{if } V_{i+1} > V_i > V_{i-1} \\ \mathbf{R}_i - \mathbf{R}_{i-1} & \text{if } V_{i+1} < V_i < V_{i-1} \end{cases}. \tag{13}$$

If image i is at an extrema along the path (*i.e.* $V_{i+1} > V_i < V_{i-1}$ or $V_{i+1} < V_i > V_{i-1}$), $\boldsymbol{\tau}_i$ is given by

$$\boldsymbol{\tau}_i = \begin{cases} (\mathbf{R}_{i+1} - \mathbf{R}_i)\,\Delta V_i^{\max} + (\mathbf{R}_i - \mathbf{R}_{i-1})\,\Delta V_i^{\min} & \text{if } V_{i+1} > V_{i-1} \\ (\mathbf{R}_{i+1} - \mathbf{R}_i)\,\Delta V_i^{\min} + (\mathbf{R}_i - \mathbf{R}_{i-1})\,\Delta V_i^{\max} & \text{if } V_{i+1} < V_{i-1} \end{cases}, \tag{14}$$

where

$$\Delta V_i^{\max} = \max\left(|V_{i+1} - V_i|\,, |V_{i-1} - V_i|\right) \tag{15}$$

$$\Delta V_i^{\min} = \min\left(|V_{i+1} - V_i|\,, |V_{i-1} - V_i|\right)\,. \tag{16}$$

Extending the NEB method by the climbing image approach enables rigorous convergence to a saddle point without compromising the MEP. For this purpose, the image along the path with the highest potential energy is designated as climbing image l, and the resulting force is adjusted by

$$\mathbf{F}_l^{\mathrm{CI}} = \mathbf{F}_l - 2 \cdot \mathbf{F}_l \hat{\boldsymbol{\tau}}_l \hat{\boldsymbol{\tau}}_l\,. \tag{17}$$

Due to the reformulation of the force projection scheme in Eq. (17), the image l undergoes no spring forces and climbs by a reflection in the forces along the tangent to the saddle point of the MEP.[51]

2.2.2 Vibration analysis

The vibrational properties of a system can be studied within the framework of the harmonic oscillator approximation. Based on the resulting vibrational modes, one can confirm transition states or calculate pre-exponential factors to determine reaction rates following the transition state theory.

In this work, we used the finite difference approximation of the Hessian matrix for the vibration analysis of an interacting atomic system.[63] For a set of N atoms and their atomic positions as a single vector $\mathbf{R} = (R_1, R_2, ..., R_{3N})$, the potential energy function can be ex-

pressed by a Taylor expansion of the atomic potential energy values around the reference geometry at $\mathbf{R}_0 = (R_{1,0}, R_{2,0}, ..., R_{3N,0})$ following

$$V = V_0 + \sum_{i}^{3N} \left.\frac{\partial V}{\partial R_i}\right|_0 (R_i - R_{i,0}) + \frac{1}{2}\sum_{i}^{3N}\sum_{j}^{3N} \left.\frac{\partial^2 V}{\partial R_i \partial R_j}\right|_0 (R_i - R_{i,0})(R_j - R_{j,0}) + ... \,. \quad (18)$$

If the system is situated in an energetic minimum or at a saddle point, the first derivation in Eq. (18) becomes zero. Further, we can define $V_0 = 0$, since this term arbitrarily shifts the total potential energy. Thus, Eq. (18) can be reformulated into a second-order Taylor polynomial as

$$V = \frac{1}{2}\sum_{i,j} \Delta R_i H_{ij} \Delta R_j = \frac{1}{2}\Delta\mathbf{R}^{\intercal}\mathbf{H}\Delta\mathbf{R} \quad (19)$$

where

$$H_{ij} = \left.\frac{\partial^2 V}{\partial R_i \partial R_j}\right|_0 = -\frac{\partial F_j}{\partial R_i} \,. \quad (20)$$

forms a $3N \times 3N$ matrix and is known as the Hessian matrix. The elements of the Hessian can be estimated by a finite difference approximation as follows:

$$H_{ij} = \left.\frac{\partial^2 V}{\partial R_i \partial R_j}\right|_0 \approx \frac{V(\delta x_i, \delta x_j) - 2V_0 + V(-\delta x_i, -\delta x_j)}{\delta x_i \delta x_j} + \mathcal{O}(\delta x_i \delta x_j) \quad (21)$$

Here, $V(\delta x_i, \delta x_j)$ was used as a shorthand notation to denote the energy of the atoms when only the specified coordinates are non-zero.[64]

The force F_j along the atomic coordinate axis j is related to Newton's equation of motion as

$$F_j = -\frac{\partial V}{\partial R_j} = M_j \frac{\mathrm{d}^2 \Delta R_j}{\mathrm{d}t^2} \,, \quad (22)$$

where M_j is the atomic mass along the j^{th} coordinate. In the more concise matrix notation, Eq. (22) yields

$$-\mathbf{H}\Delta\mathbf{R} = \mathbf{M}\frac{\mathrm{d}^2\Delta\mathbf{R}}{\mathrm{d}t^2} \,. \tag{23}$$

Herein, the constructed Hessian $\mathbf{H}$ is real and symmetric and has a complete set of $3N$ eigenvectors $\mathbf{e}_1, ..., \mathbf{e}_{3N}$. Moreover, $\mathbf{M}$ denotes the diagonal matrix of the atomic masses. We can solve the equation of motion (23) by a linear combination of the normal modes $\mathbf{R}_k(t) = \mathbf{a}_k \exp(-\mathrm{i}\omega_k t)$, which take the form:[63]

$$\mathbf{H}\mathbf{R}_k = \omega_k^2 \mathbf{M}\mathbf{R}_k \tag{24}$$

The vibrational frequencies and mass-weighted vibrational modes can be determined from the solution of the eigenvalue equation $\mathbf{A}\mathbf{e} = \lambda\mathbf{e}$ with the mass-weighted Hessian $\mathbf{A} = \mathbf{M}^{-1/2}\mathbf{H}\mathbf{M}^{-1/2}$. We can calculate the $3N$ vibrational frequencies ν from the obtained eigenvalues λ as

$$\nu_i = \frac{\sqrt{\lambda_i}}{2\pi} \,. \tag{25}$$

Subsequently, the zero-point energy E_{ZPE} can be determined from the sum of the calculated normal mode frequencies following

$$E_{\text{ZPE}} = \sum_{i=1}^{3N} \frac{h\nu_i}{2} \,, \tag{26}$$

where h is the Planck constant.

2.2.3 Force-based optimisers

Polak-Ribière conjugate gradient (CG) – The CG optimiser is a local optimisation algorithm that performs a line search along a conjugate search direction.[51,59,60]

At the beginning of the optimisation routine, the initial search direction $\mathbf{d}_0$ along the initial force $\mathbf{F}_0$ is defined following

$$\mathbf{d}_0 = \mathbf{F}_0 \ . \tag{27}$$

Applying the step size λ and the current conjugate search direction $\mathbf{d}_j$, the new atomic positions $\mathbf{R}_{j+1}$ of iteration $j+1$ are calculated as

$$\mathbf{R}_{j+1} = \mathbf{R}_j + \lambda \mathbf{d}_j \ . \tag{28}$$

In the following iterative steps, the new conjugate search direction $\mathbf{d_{j+1}}$ is calculated from the current negative gradient $\mathbf{F}_{j+1}$ and the search direction $\mathbf{d}_j$ of the j^{th} iteration as follows

$$\mathbf{d_{j+1}} = \mathbf{F}_{j+1} + \gamma^{\text{PR}} \mathbf{d}_j \ , \tag{29}$$

where

$$\gamma^{\text{PR}} = \frac{\mathbf{F}_{j+1} \cdot (\mathbf{F}_{j+1} - \mathbf{F}_j)}{|\mathbf{F}_j|^2} \tag{30}$$

All steps from Eq. (29) and (30) are repeated iteratively until the specified termination criterion is met.

Fast inertial relaxation engine (FIRE) – The FIRE optimiser is a simple local atomic structure optimisation algorithm based on classical molecular dynamics (MD) with adaptive time steps and a modified velocity formulation.[58] It is characterised by its robustness, versatility and overall performance. For the propagation of the optimisation trajectory, either a classical velocity Verlet algorithm can be utilised, or an Euler integration can be performed. Initially, a time step Δt and a velocity damping constant $\alpha = \alpha_{\text{start}}$ are provided as well as the velocity vector $\mathbf{v}$ is set to zero.

In an MD step, forces and velocities are determined for a given set of atomic positions $\mathbf{R}$ following

$$\mathbf{v} = \left(\mathbf{v} \cdot \hat{\mathbf{F}}\right) \hat{\mathbf{F}} \tag{31}$$

$$\mathbf{F} = -\nabla V(\mathbf{R}) \, . \tag{32}$$

Next, the force P is calculated according to

$$P = \mathbf{F} \cdot \mathbf{v} \, , \tag{33}$$

and a new velocity vector is generated from the existing velocity and force vector following

$$\mathbf{v} \rightarrow (1 - \alpha) \, \mathbf{v} + \alpha \cdot \hat{\mathbf{F}} \, |\mathbf{v}| \ . \tag{34}$$

Lastly, the time step Δt and the velocity damping constant α are dynamically adjusted. If the force $P > 0$ and the number of steps since P was negative is greater than $N_{\min}$ (number of iterations before a and dt are updated), the values are adapted as follows:

$$\Delta t \rightarrow \min(\Delta t \cdot f_{\text{inc}}, \Delta t_{\max}) \tag{35}$$

$$\alpha = \alpha \cdot f_{\alpha} \, . \tag{36}$$

In the case of $P \leq 0$, the velocity is set to v=0, and the parameters are modified according to

$$\Delta t \rightarrow \Delta t \cdot f_{\mathrm{dec}} \tag{37}$$

$$\alpha = \alpha_{\mathrm{start}} \ , \tag{38}$$

where Δt_{max} is the maximum dynamical time step and f_{inc} and f_{dec} are factors to increase and decrease the time step Δt.

Starting with the MD step, the described steps are repeated iteratively until the termination criterion is reached. In general, a robust and stable optimisation behaviour has been found using $N_{\mathrm{min}} = 5$, $f_{\mathrm{inc}} = 1.1$, $f_{\mathrm{dec}} = 0.5$, $\alpha_{\mathrm{start}} = 0.1$, and $f_{\alpha} = 0.99$ as initial parameters.[58]

Limited-memory Broyen-Fletcher-Goldfarb-Shanno (L-BFGS) – The L-BFGS optimiser is a quasi-Newton method utilising the inverse Hessian $\mathbf{H}^{-1}$ of the system to optimise the atomic structure. However, the determination of the complete second derivative matrix can be computationally expensive compared to the calculation of the gradient. Therefore, in the limited-memory quasi-Newton methods, only a few vectors of size n are saved instead of the dense $n \times n$ matrices.[65] Starting from a diagonal matrix, the Hessian is constructed using the curvature information from the most recent iterations. Further information regarding the construction of the matrices can be found in Ref.[61] and.[65]

In the next step of the optimisation procedure, the new atomic positions $\mathbf{R}_{j+1}$ of iteration $j+1$ are determined based on the system's approximated inverse Hessian matrix $\mathbf{H}_j^{-1}$.

Using the L-BFGS(line) method, the search direction $\mathbf{d}_j$ is determined by

$$\mathbf{d}_j = \mathbf{F}_j \mathbf{H}_j^{-1} \ , \tag{39}$$

and the new coordinates are calculated following

$$\mathbf{R}_{j+1} = \mathbf{R}_j + \lambda \mathbf{d}_j \ . \tag{40}$$

Alternatively, the L-BFGS(Hess) method can be used to obtain $\mathbf{R}_{j+1}$ directly using the inverse Hessian as follows:

$$\mathbf{R}_{j+1} = \mathbf{R}_j + \mathbf{F}_j \mathbf{H}_j^{-1} \ . \tag{41}$$

Only one force call per iteration is needed in the latter, as the finite difference step to calculate the step size λ is omitted. However, a poor initial guess of $\mathbf{H}^{-1}$ for the LBFGS(Hess) approach can lead to oscillations or arbitrary behaviour and thus retard convergence substantially.[51]

3 Benchmark Function Experiments

For a deeper understanding of the performance and behaviour of the different evolutionary algorithms, we evaluated their performance and behaviour against mathematical benchmark functions. For our performance test of the evolutionary algorithms, we have selected the functions Ackley, Alpine N.1, Rastrigin, Rosenbrock, Schwefel and Xin-She Yang N.4[66] to capture a wide variety of functional properties. This set of benchmark functions has been chosen based on their complexity, continuity, modality and convexity. Their functional form and properties are summarised in Appendix B.

All benchmark function experiments were performed with a total population size of 50 and a maximum iteration number of 10000. If the difference between fitness and target value was less than 1×10^{-8}, the calculation was considered converged. An ensemble of 100 search runs was generated to enhance the statistical significance of the result. For all CPSO calculations, the parameters $\gamma = 1$, $\phi_{\mathrm{p}} = \phi_{\mathrm{g}} = 1.49618$, and $\omega = 0.7298$ were used. A mutation constant of $F = 0.5$ and a crossover constant of $CR = 0.9$ were taken in the case of the DE algorithm. The '*best1bin*' differential evolution strategy (compare with Eq. (7)) was applied, following

$$\mathbf{v}_{i,G+1} = \mathbf{x}_{\text{best},G} + F\left(\mathbf{x}_{r_1,G} - \mathbf{x}_{r_2,G}\right), \quad F \in [0,2],\ r_1, r_2 \in \{1, .., N_\text{P}\}\ , \tag{42}$$

where $\mathbf{x}_{\text{best},G}$ is the best vector found at generation G, and r_1, r_2 ($r_1 \neq r_2$) are random indices. A synchronous update scheme was used for both CPSO and DE, *i.e.* the best solution vector was constantly updated within a single generation.

For the CMA-ES optimisation procedure, 50 % of the total population were defined as parents, and an initial standard deviation of $\sigma = 0.1$ was chosen. The generated output from the evolutionary algorithms was compared with the data of the sequential one-parameter parabolic interpolation (SOPPI) approach. In the latter, a step size of ± 10 % of the parameter range was adopted for the parabolic fit. In all methods, constraints were applied to keep the parameter search space within the specified boundaries.

Table 1 summarises the obtained results of CPSO, DE, CMA-ES, and SOPPI for different d-dimensional parameter spaces. Further, supplementary data for classical PSO, VD-CMA algorithm, additional benchmark functions, and findings for different parameter settings are provided in Appendix C.

The Ackley function[67,68] is a continuous, non-convex, and multimodal function with a global minimum at $f(0, ..., 0) = 0$. It is characterised by a relatively flat area with numerous local minima surrounding the global minimum in the centre. While the CPSO and CMA-ES algorithms identified the global minimum for different dimensional spaces with great statistical accuracy, DE and SOPPI tended to get trapped in local minima.

In the case of the DE approach, altering the differential evolution strategy can overcome this issue (see Appendix C - Table 22). The *rand1bin* and *rand2bin* strategies utilise random parent vectors in the generation of the mutation vector. This improves the exploration capability of the algorithm but may slow down convergence. Further, the *rand2bin* strategy introduces an additional difference vector, which enhances the perturbation. For the strategies *best1bin* and *best2bin*, the best solutions of the parent population are used to generate the mutation vector, which allows faster convergence to the optimal solution, but bears the

Table 1: Global performance of the evaluated evolutionary algorithms (CPSO, DE, CMA-ES, SOPPI) for different d-dimensional benchmark functions. The calculations were carried out using a total population of 50, with 10000 maximum iterations. All values (mean $\pm$ standard deviation) were determined using an ensemble of 100 calculations per system. For all test functions, the global minimum is 0, except Xin-She Yang N.4 with a value of $-d$.

Function	d	CPSO	DE	CMA-ES	SOPPI
Ackley	2	0.00 ± 0.00	0.00 ± 0.00	3.38 ± 7.46	6.55 ± 9.34
	4	0.00 ± 0.00	0.04 ± 0.26	3.16 ± 7.24	3.97 ± 7.95
	8	0.00 ± 0.00	1.32 ± 1.39	1.58 ± 5.34	4.58 ± 8.39
	16	0.00 ± 0.00	4.10 ± 1.95	0.59 ± 3.36	3.19 ± 7.31
	32	0.00 ± 0.00	10.04 ± 1.97	0.00 ± 0.00	1.20 ± 4.74
Alpine N.1	2	0.00 ± 0.00	0.00 ± 0.00	0.00 ± 0.00	1.06 ± 0.82
	4	0.00 ± 0.00	0.00 ± 0.00	0.00 ± 0.00	2.46 ± 1.35
	8	0.00 ± 0.00	0.00 ± 0.00	0.00 ± 0.00	5.71 ± 1.86
	16	0.00 ± 0.00	0.01 ± 0.06	0.00 ± 0.00	11.49 ± 2.92
	32	0.00 ± 0.00	0.05 ± 0.41	0.03 ± 0.23	23.96 ± 4.20
Rastrigin	2	0.00 ± 0.00	0.20 ± 0.40	2.19 ± 5.01	13.89 ± 5.24
	4	0.00 ± 0.00	2.12 ± 1.96	3.46 ± 6.26	33.41 ± 6.33
	8	0.02 ± 0.14	9.59 ± 4.12	3.43 ± 3.65	75.31 ± 8.96
	16	0.30 ± 1.71	29.30 ± 9.28	7.20 ± 8.32	167.38 ± 12.70
	32	11.58 ± 12.55	69.70 ± 18.01	17.04 ± 3.58	356.11 ± 17.04
Rosenbrock	2	0.00 ± 0.00	0.00 ± 0.00	0.00 ± 0.00	0.35 ± 0.35
	4	0.07 ± 0.52	0.74 ± 1.48	0.00 ± 0.00	2.79 ± 0.27
	8	0.28 ± 1.02	0.88 ± 1.65	0.00 ± 0.00	6.83 ± 0.07
	16	2.16 ± 16.57	0.84 ± 1.62	0.00 ± 0.00	14.81 ± 0.06
	32	1.24 ± 2.00	1.40 ± 1.90	0.04 ± 0.40	30.75 ± 0.05
Schwefel	2	0.00 ± 0.00	36.72 ± 61.99	278.31 ± 157.66	100.86 ± 91.65
	4	23.69 ± 47.38	148.25 ± 118.23	577.05 ± 239.85	208.31 ± 136.81
	8	309.12 ± 143.01	685.19 ± 255.66	1321.71 ± 345.02	452.17 ± 227.30
	16	753.40 ± 258.27	2142.52 ± 448.43	2832.63 ± 511.23	929.01 ± 321.70
	32	1838.26 ± 366.55	5758.91 ± 638.37	5780.52 ± 695.61	1998.98 ± 458.99
Xin-She Yang N.4	2	-1.99 ± 0.01	-1.99 ± 0.01	-0.92 ± 0.87	-0.31 ± 0.32
	4	-3.93 ± 0.18	-3.36 ± 1.00	-2.31 ± 1.71	-0.13 ± 0.16
	8	-7.39 ± 1.39	-6.34 ± 2.30	-7.11 ± 1.59	-0.04 ± 0.09
	16	-10.40 ± 3.93	-10.37 ± 4.56	-12.33 ± 3.82	-0.00 ± 0.03
	32	-23.46 ± 7.39	-22.36 ± 7.46	-20.20 ± 7.07	-0.00 ± 0.00

risk of getting stuck in a local minimum in the case of multimodal functions.[69] As shown in Table 22, applying the *rand1bin* or *rand2bin* differential evolution strategy yields a robust identification of the global solution of Ackley's function. The performance of the SOPPI approach can be improved by decreasing the step size gradually during the optimisation process. In our case, an initial step length of $\delta = 0.1$ or $\delta = 0.05$ and a reduction of 1 % every 10 iterations (down to a minimum value of $\delta = 0.005$) provided the model's best solution consistently (see Appendix C - Table 32).

Alpine N.1 is a non-continuous, non-convex, and multimodal function with one global minimum at the margin of the definition range at $f(0, ..., 0) = 0$. Here, the model parameter space was designed in the shape of a descending mountain landscape with multiple local minima in the valleys. Unlike Ackley's function, Alpine N.1 is not differentiable and possesses a far lower density of local extrema. The EAs found the global minimum reliably in this benchmark run, even for high-dimensional parameter spaces. As expected, searches with SOPPI often ended in local minima. However, using a decreasing step length to find the best solution of the d-dimensional function improved the performance considerably.

Due to its numerous, regularly distributed local minima and large search space, the widely used Rastrigin function[70,71] have been a severe challenge to many optimisation techniques. The continuous, non-convex, and highly multimodal function has a global minimum at $f(0, ..., 0) = 0$ with multiple surrounding local minima whose function value grows with increasing distance from the centre. Although the Rastrigin function entails fewer minima within the defined search space, its overall shape is shallower than Ackley's function, making general convergence to the global optimum more severe.

For this single-objective optimisation test function, the diversity of the swarm and the continuous sampling of the parameter space of the CPSO come into play. The search converges to the best solution with high statistical confidence, except for the high-dimensional parameter spaces, where the swarm tends to get caught in a local minimum. For the latter, the performance can be improved by enlarging the swarm size or increasing the competitivity

parameter γ (see Appendix C - Table 18 and 20). Both DE and CMA-ES struggle to reach the global minimum even for the low dimensional variants of the Rastrigin function. Similarly to Ackley's function, applying the *rand1bin* differential evolutionary strategy yields a significant improvement in the search performance of the DE routine.

Applying a fixed step length ($\delta = 0.1$, $\delta = 0.05$, and $\delta = 0.01$) during the SOPPI optimisation runs achieved the worst results of all tested algorithms. However, assuming an initial step length of $\delta = 0.1$ and a reduction of 1 % every 10 iterations, the variable SOPPI approach was able to keep up with the performance of CPSO and even outperform it in the 32-dimensional parameter space (see Appendix C - Table 32).

The continuous, non-convex Rosenbrock function[72] is unimodal ($d \leq 2$) or multimodal ($d > 2$), and has a parabolic shape and a flat valley bottom (2-dimensional case). Locating the valley is facile, but finding the off-centre global minimum at $f(1, ..., 1) = 0$ is demanding for many optimisation routines.[73,74] For the unimodal variant ($d = 2$) of the function, the evolutionary algorithms are able to locate the global minimum of the function correctly. While the CMA-ES also converges to the optimal solution for the higher-dimensional parameter spaces, both CPSO and DE have difficulties identifying the global minimum. In the case of CPSO, altering the swarm size or the competitivity parameter γ provided no significant improvement. The search results of the DE algorithm can be refined by utilising the *rand1bin* and *rand2bin* strategies. For the Rosenbrock benchmark test, SOPPI achieved the worst scores. Modifying the parameters of the optimiser showed no remarkable improvement.

The Schwefel benchmark test consists of a continuous, non-convex and multimodal function with a global best solution at the boundary of the search space with a minimum value of $f(420.9687, ..., 420.9687) = 0$. Contrary to Rastrigin's or Ackley's function, the Schwefel function[75] is less symmetric and does not provide an overall guiding slope towards the global minimum. In the search for the global minimum, the CPSO approach demonstrates superior performance with respect to the other optimisation routines due to its high swarm diversity.

For the DE algorithm, the exploration capability can be significantly improved by adopting the *rand1bin* strategy to generate the mutation vector. This strategy change results in the overall best performance for Schwefel's function, as shown in Appendix C - Table 22. For a fixed step length of $\delta = 0.1$, the optimisation runs with SOPPI perform surprisingly well; however, the overall results indicate a high parameter sensitivity.

Xin-She Yang N.4[76,77] is a non-continuous, non-convex and multimodal function with a global minimum at $f(0, ..., 0) = -d$. Its properties are similar to Schwefel's and Rastrigin's functions. For the 2-dimensional variant, the centroidal optimum is intersected by a canyon-like structure with deep funnel-shaped local minima. Hence, converging to the global best solution is rather difficult without getting trapped in a local minimum.

In this benchmark test, the CPSO achieved the best performance of all tested optimisation approaches. Altering the optimisation parameters or the swarm size had no significant influence on the result. For the CMA-ES, a significant improvement was reached through an increased population size. As in previous tests, the data from the DE algorithm indicated a great dependence on the chosen differential evolution strategy. The optimisation runs with SOPPI ($\delta = 0.10$) consistently ended in local minima with function values close to 0. It was possible to improve the outcome by downsizing or a gradual reduction of the step size but still failed to reach the performance level of the evolutionary algorithms.

The global optimisation performance of the tested algorithms for the 32-dimensional variant of Ackley, Rastrigin, Rosenbrock, and Schwefel is given in Fig. 1. The SOPPI approach proves to be an efficient optimisation method with a fast convergence after only a few algorithm iterations. For multimodal functions, however, we found a strong tendency to get trapped in a local minimum. Applying a varying step size improved the result notably for some test functions but revealed a high sensitivity regarding the chosen optimisation settings. While for SOPPI, only three evaluations of the objective function per optimisable parameter and iteration are required, the number of calls is equal to the population size of the evolutionary algorithm. However, the latter can be easily parallelised and scales al-

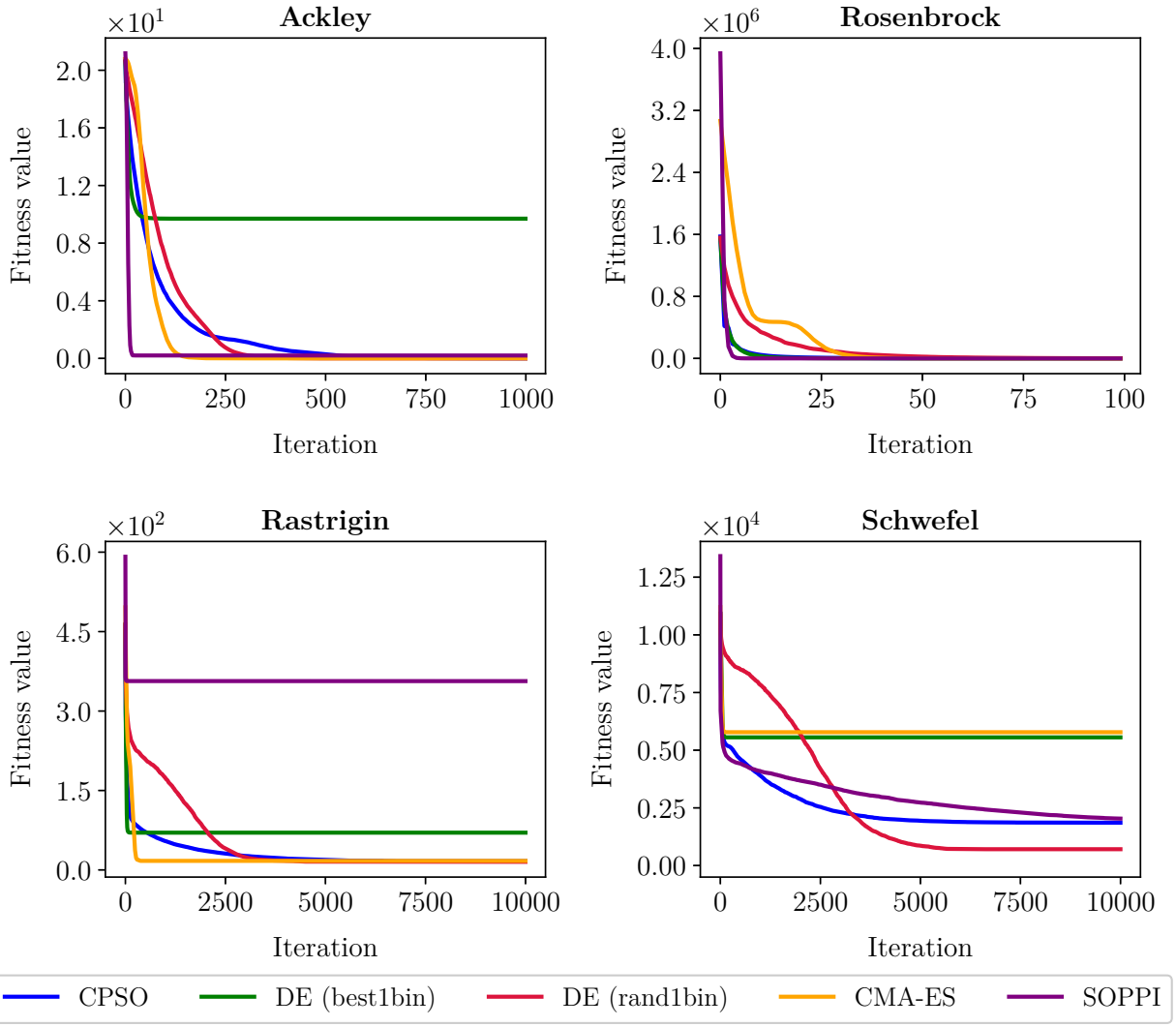

Figure 1: Global optimisation performance of CPSO (blue), DE (*best1bin*) (green), DE (*rand1bin*) (red), CMA-ES (orange), and SOPPI (purple) in the 32-dimensional parameter space of Ackley (upper left), Rosenbrock (upper right), Rastrigin (lower left), and Schwefel (lower right). For all calculations, 10,000 algorithm iterations were performed, and an ensemble of 100 searches was generated to enhance the statistical significance of the results. The population size was set to 50 for all evolutionary algorithms and a step size of $\delta = 0.1$ for the SOPPI method.

most linearly with the number of cores.[78–81] Modern multiprocessor architectures are readily suited to compensate for the potential higher computational demands of the EAs.

The CPSO proves to be highly robust but requires more iterations on average to reach a state of convergence. It was possible to obtain reliable results even for smaller swarm sizes. Also, this method proved to be relatively insensitive to the selected parameters. In the case of the DE algorithm, the *best1bin* strategy was able to achieve fast convergence but had a tendency to get caught in local minima of multimodal functions. Changing the differential evolutionary strategy from *best1bin* to *rand1bin* may increase the number of function evaluations but help to more reliably find the global minimum. For CMA-ES, a vastly improved result was found after only a few iterations. Still, high-complex benchmark functions such as *Schwefel* or *Xin-She Yang N.4* bore a high risk of premature convergence.

4 Force field development: optimisation and validation

A training set based on quantum mechanical or experimental data is needed to optimise and validate a reactive force field. The classical ReaxFF training set is organised in five segments: Atomic charges, forces, cell parameters, energy differences, and heat of formation. These values are compared to the calculated results for the current ReaxFF parameter set j, and the associated error function ϕ_j^{ReaxFF} is determined as

$$\phi_j^{\mathrm{ReaxFF}} = \sum_{i=1}^{n} \left[\frac{x_i^{\mathrm{Ref}} - x_{j,i}^{\mathrm{ReaxFF}}}{\sigma_i} \right]^2 , \tag{43}$$

where x_i^{Ref} is the reference value, $x_{j,i}^{\mathrm{ReaxFF}}$ is the computed value, and σ_i is the weight value of the optimisation target i.

While the classical training set is well suited for the training of molecules, there are some restrictions on integrating surface properties. Depending on the ReaxFF parameter set, the lattice constant of the bulk phases may vary with respect to the reference data. Yet, the minimum lattice constant change is not taken into account for the surface structures within

the training set. In this way, the introduced lattice strain can influence fundamental surface quantities[82] and thus may distort the error function. Moreover, due to the lack of constraint options, the description of metastable or unstable surface sites is limited. In a classical training set, the images of a minimum energy path or the data of a potential energy scan are typically included in the form of a single point calculation or by applying bond, angle, or torsion restraints. However, an accurate representation of the potential energy surface (PES) is crucial for the description of the surface kinetics.

To overcome these limitations, we developed a new training routine for solid-state systems and their surface properties. A general workflow of the extended training routine is given in Fig. 2.

For a given set of parameters, we initially optimise the different bulk phases of the system and compute the respective equation of states (EOS). From these calculations, the minimum volume V_0, the lattice parameters (a_0, b_0, c_0, α_0, β_0, γ_0), the cohesive energy E_{coh}, energy differences ΔE and the bulk modulus B_0 are obtained. Next, the different surface structures are generated based on the minimum lattice parameters of the given parameter set. Apart from the surface energies γ_{hkl} of the different facets, the energetics (adsorption energies E_{ad}, dimer interaction energies $E_{\mathrm{int,dimer}}$) of the characteristic adsorption sites and the coverage-dependent adsorption are analysed. Due to the newly implemented force-based optimiser, it is possible to fix some degrees of freedom in the system, enabling simple integration of metastable and unstable surface structures into the training. Following the terrace-step-kink model,[83] we use well-chosen diffusion processes to train the surface kinetics. Their minimum energy paths and activation energies ($E_{\mathrm{a}}^{\mathrm{for}}$ (forward), $E_{\mathrm{a}}^{\mathrm{rev}}$ (reversed)) are computed utilising NEB calculations. Finally, the vibrational frequencies ν_i are determined for the initial, transition, and final state to derive the pre-exponential factors k_0^{for} and k_0^{rev}.

All obtained quantities are referenced against the training set data to calculate the error value for the given parameter set using the error function defined in Eq. (43). We repeat this procedure for each new parameter set until an appropriate termination criterion is reached.

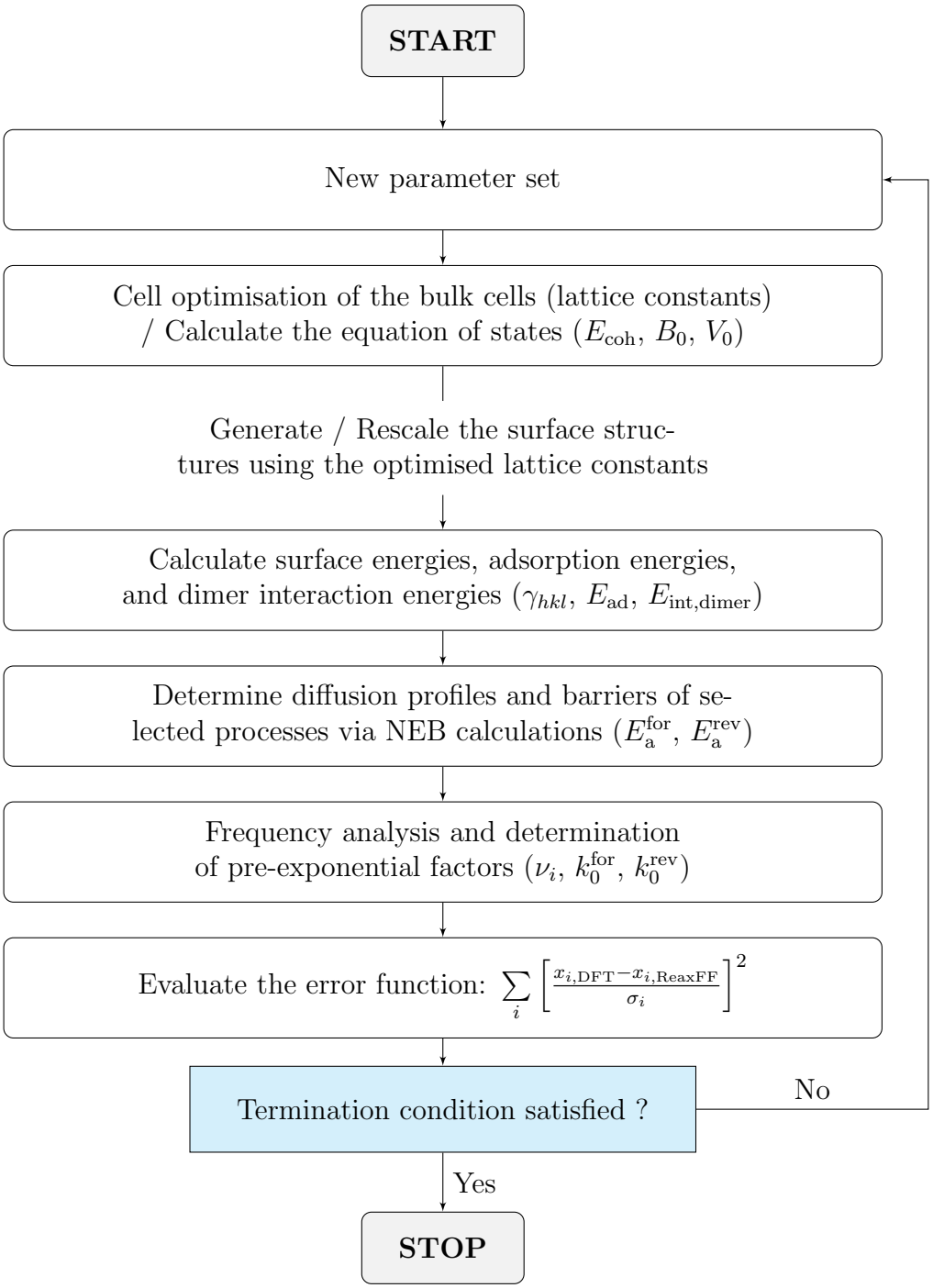

Figure 2: General workflow of the developed ReaxFF training routine for the optimisation of (metallic) solid-state systems and their surface properties.

Possible criteria are the solution tolerance, the objective function value tolerance or the maximum algorithm iterations. Our developed force field parametrisation routine supports the evolutionary algorithms PSO, CPSO, DE, CMA-ES, and VD-CMA of the python library

for stochastic numerical optimisation.[84]

The outlined optimisation framework for EA-based parameterisation of ReaxFF reactive force field potentials is dubbed *KVIK* (*Icelandic for: dynamic, in motion*). The training routine can be extended by user-defined quantities and is fully interoperable with classical training set files.

Part II: Development and application of a ReaxFF force field for solid systems

In order to show the applicability to solid systems, in this part the developed *KVIK* approach will be utilised to optimise a reactive force field potential for metallic sodium and lithium and their interaction. For this purpose, the proposed training set will be generated with the data from our previous work.[85,86] Subsequently, a multi-scale model will be applied to investigate the initial growth processes on the stable surfaces of both metals using kMC simulations. The required activation energies and pre-exponential factors of the respective processes will be calculated utilising the developed reactive force field potential. For these systems, the major challenge in optimising the force field parameters is the subtle energetic differences between the various diffusion processes. Hence, an accurate description of the diffusion properties is vital for properly describing the surface growth.

5 Computational details

5.1 DFT calculations

All electronic structure calculations were carried out using the Vienna Ab initio Simulation Package (VASP).[87,88] Electron-core interactions were accounted for by the projector augmented wave (PAW) method[89] in the implementation of Kresse and Joubert.[90] Exchange-correlation effects were described by the functional of Perdew, Burke, and Ernzerhof (PBE)

in the generalised gradient approximation (GGA).[91] Respective standard deviations were computed utilising the Bayesian error estimation functional with van-der-Waals (BEEF-vdW) exchange-correlation functional.[92] Following the scheme of Monkhorst and Pack,[93] all total energy calculations were done using a k-point mesh density of $0.15\,\text{Å}^{-1}$. A plane-wave cutoff energy of 340 eV was applied for the expansion of the electron one-particle wave functions into a plane-wave basis set. The DFT calculations were considered as converged when the total energy difference was less than 10^{-5} eV and all forces exceeded a threshold of $10^{-3}\,\text{eV}\,\text{Å}^{-1}$. Images of CI-NEB calculations[49,50] were separated by a spring constant of $5.0\,\text{eV}\,\text{Å}^{-2}$ to guarantee the continuity of the path. Surface properties were modelled within the supercell approach introducing a vacuum region of at least 20 Å along the z-axis. Well converged symmetrical slabs with a minimum thickness of 20 Å were used to compute the respective surface energies. To examine the adsorption and diffusion properties on (100)-, (110)- and (111)-indexed surface models, 8-, 8- and 13-layer slabs were used, respectively. The two lowermost layers of the (100) and (110) surface structures and the three lowermost layers of Na(111) and Li(111) were kept fixed in their respective bulk atomic configuration.

5.2 ReaxFF parameterisation and calculations

In this work, all reactive force field calculations were performed within the ReaxFF implementation of the Amsterdam Modeling Suite 2021.1.[1,2,94] The developed ReaxFF parameter set for Li-Li, Li-Na, and Na-Na interactions is provided in Appendix D. Geometry optimisations, NEB calculations, and frequency analyses were performed within the framework of the Transition State Tools for ReaxFF (see Appendix A). For an efficient calculation of atomic charges and linear response properties, the atom-condensed Kohn-Sham density functional theory approximated to second order (ACKS2)[4,95] charge equilibration scheme was applied. Energy minimisation of the atomic coordinates was considered converged when all forces were smaller than $2 \times 10^{-3}\,\text{eV}\,\text{Å}^{-1}$. For NEB calculations, a spring constant of $5.0\,\text{eV}\,\text{Å}^{-2}$ and a convergence criterion of $1 \times 10^{-2}\,\text{eV}\,\text{Å}^{-1}$ were chosen. A displacement value of 0.01 Å

with four displacements per spatial direction was used to compute the respective vibrational modes.

Depending on the selected dimensionality and boundary conditions, the evolutionary algorithms CPSO and DE, as implemented in the stochopy package,[84] were adopted for the force field parameter fitting. The swarm size was adjusted according to the number of parameters to be optimised. For all CPSO calculations, the parameters $\gamma = 1$, $\phi_\mathrm{p} = \phi_\mathrm{g} = 1.49618$, and $\omega = 0.7298$ were chosen. In optimisation runs with the DE algorithm, the '*best2bin*' differential evolution strategy (see Appendix C.4) was used with a mutation constant of $F = 0.5$ and a crossover constant of $CR = 0.9$.

5.3 Grand Canonical Monte Carlo

All grand canonical Monte Carlo (GCMC) simulations were carried out in the AMS-ReaxFF implementation of the Amsterdam Modeling Suite 2021.1.[1,2,94] The chemical potential μ was referenced to the cohesive energy of the respective metal using a simulation temperature of 300 K. Also, an μVT ensemble was chosen for all GCMC simulations. A minimum distance of 1.0 Å and a maximum distance of 3.0 Å to the other atoms of the system were set as boundary conditions for adding an atom. The accessible volume was determined by the difference between the total and occupied volumes.

5.4 Kinetic Monte Carlo

All kinetic Monte Carlo (kMC) simulations were performed within the ReaxFF implementation of the Amsterdam Modeling Suite 2021.1.[1,2,94] A 100x100 Li(100) and Na(100) slab was utilised to simulate the initial growth processes applying periodic boundary conditions in x- and y-directions. In all simulations, the maximum number of iterations was set to 1×10^9. The diffusion constants were determined from an ensemble of 20 kMC calculations to increase the statistical significance of the results.

6 Results and Discussion

6.1 Training and validation of Li-Li and Na-Na interaction

In the following, the computed ReaxFF data for sodium and lithium are compared with the DFT-PBE target values. We refer the reader to our previous work[85,86] for a detailed discussion of their bulk and surface properties. Moreover, a side-by-side comparison of known ReaxFF force fields for Li[96–98] is given in Appendix E.

Bulk phases – The ReaxFF force field potential describing the Li-Li and Na-Na interactions was obtained by optimising the relevant empirical force field parameters within the KVIK optimisation framework. Besides the structural and energetic properties of the relevant bulk phases, the training set also includes their volumetric compression and expansion characteristics. An overview of the obtained bulk properties is given in Table 2.

Table 2: Calculated (ReaxFF, DFT-PBE) physical constants for the important bulk phases of sodium and lithium. Lattice constant a_0 and c_0 are given in Å, cohesive energy values E_{coh} are given in eV atom^{-1}, and bulk moduli B_0 are given in GPa. All experimental results were taken from Ref.[99] and the DFT-PBE values are taken from our previous work.[85,86] The determined standard deviation[86] from the BEEF-vdW[92] calculations are given in brackets.

		Sodium			Lithium		
		ReaxFF	DFT-PBE	Expt.	ReaxFF	DFT-PBE	Expt.
bcc	a_0	4.18	4.19	4.21	3.42	3.44	3.45
	E_{coh}	1.10	1.09 (0.25)	1.13	1.61	1.61 (0.16)	1.67
	B_0	8.13	7.96	7.73	12.99	13.92	13.90
fcc	a_0	5.33	5.29	-	4.33	4.33	-
	E_{coh}	1.09	1.09 (0.25)	-	1.60	1.61 (0.16)	-
	B_0	7.74	7.87	-	14.22	13.86	-
hcp	a_0	3.77	3.74	-	3.05	3.06	-
	c_0	6.15	6.11	-	4.98	5.00	-
	E_{coh}	1.09	1.09 (0.25)	-	1.60	1.61 (0.16)	-
	B_0	6.72	7.91	-	9.94	13.87	-
hR9	a_0	3.76	3.72	-	3.07	3.07	-
	c_0	27.83	27.80	-	22.32	22.33	-
	E_{coh}	1.09	1.09 (0.25)	-	1.60	1.61 (0.16)	-
	B_0	6.73	7.84	-	9.94	13.97	-

The bulk modulus B_0 was determined by a third-order inverse polynomial fit according to the stabilised Jellium equation of state (SJEOS).[100,101] All lattice constants (a_0, c_0) and cohesive energy values (E_{coh}) were obtained from the individual cell and geometry optimised structure.

Our parameterised potential function can correctly reproduce the stability sequence of the respective sodium and lithium bulk phases. Moreover, we found excellent agreement between the structural and energetic data from DFT-PBE and ReaxFF. For the respective bulk moduli, minor deviations of a few GPa could be observed; however, their fluctuations are within the error range of the DFT.[86] Although the low-temperature phase *hr9* was not included in the training set, the crystal structure is correctly reproduced by ReaxFF. This indicates a good transferability of the developed parameter set.

Surface properties – In order to enable a thermodynamically accurate description of crystal growth phenomena, the stabilities of the individual facets have to be predicted properly. Hence, we considered the surface energy of the low-index surfaces (100), (110), and (111) in the force field parameter training to ensure accurate description through the potential function. The surface energies of additional unreconstructed Miller-index surfaces were computed to demonstrate the general applicability of the proposed parameter set to Na and Li surface structures. In this context, we defined the surface energy γ as the excess surface free energy per unit area following

$$\gamma = \frac{E_{\mathrm{slab}} - N \cdot E_{\mathrm{bulk}}}{2 \cdot A} \,, \tag{44}$$

where E_{slab} is the total energy of the slab, E_{bulk} is the bulk energy per atom, A is the surface area, and N is the number of atoms per supercell.[102] The calculated energy values of the low-index surfaces for sodium and lithium are given in Table 3.

Our parameterised potential function is capable of determining the stability sequence of the low-index surfaces for both metals correctly. While for metallic lithium, all values are within the standard deviation of the DFT data, the surface energies for sodium are slightly

Table 3: Theoretical (ReaxFF, DFT-PBE) and experimental surface energies for different surfaces of sodium and lithium. The calculated standard deviation[86] of the respective surface is given in parentheses. Experimental values are from Ref.[103] and.[104] Surface energies and standard deviations of the respective low-index surfaces (i.e. (100), (110), and (111)) were taken from Ref.[85] and.[86] All values are reported in $\mathrm{J\,m^{-2}}$.

	Sodium			Lithium		
	ReaxFF	DFT-PBE	Expt.	ReaxFF	DFT-PBE	Expt.
γ_{100}	0.178	0.247 (0.043)	-	0.484	0.473 (0.076)	-
γ_{110}	0.174	0.246 (0.039)	0.260, 0.261	0.492	0.499 (0.075)	0.522, 0.525
γ_{111}	0.204	0.271 (0.043)	-	0.564	0.542 (0.080)	-
γ_{210}	0.183	0.250 (0.045)	-	0.509	0.514 (0.077)	-
γ_{211}	0.191	0.257 (0.042)	-	0.540	0.555 (0.079)	-
γ_{221}	0.198	0.259 (0.040)	-	0.554	0.545 (0.076)	-
γ_{310}	0.184	0.249 (0.044)	-	0.507	0.517 (0.077)	-
γ_{311}	0.191	0.267 (0.047)	-	0.526	0.537 (0.079)	-
γ_{320}	0.181	0.248 (0.042)	-	0.506	0.511 (0.076)	-
γ_{321}	0.190	0.250 (0.041)	-	0.537	0.545 (0.076)	-
γ_{322}	0.200	0.264 (0.043)	-	0.556	0.551 (0.080)	-
γ_{331}	0.193	0.258 (0.040)	-	0.537	0.537 (0.075)	-
γ_{332}	0.201	0.268 (0.044)	-	0.553	0.538 (0.079)	-

downshifted by approximately $0.06\,\mathrm{J\,m^{-2}}$. Nevertheless, the obtained data for both metal systems are internally consistent. Evidently, the developed force field can be applied to a wide range of metallic sodium and lithium surfaces. For both metals, the stabilities of the stepped surface structures are well reproduced and emphasise the transferability of the parameter set.

Adsorption properties – Additionally to the bulk and surface structures, the respective adsorption energy of the atomic species on the different adsorption sites of the low-index surfaces was used to optimise the Li-Li and Na-Na interactions. We also included the energy differences between the individual positions to reproduce the surface's thermodynamics correctly. The adsorption energy per atom E_{ad} was calculated according to

$$E_{\mathrm{ad}} = E_{\mathrm{tot}} - (E_{\mathrm{slab}} + E_{\mathrm{atom}})\,, \tag{45}$$

where E_{tot} is the total energy of the interacting system, E_{slab} is the total energy of the adsorbate-free surface slab, and E_{atom} is the energy of the free-atom reference. Table 4 summarises the calculated energy values of ReaxFF and DFT-PBE.

Table 4: Calculated adsorption energies (ReaxFF, DFT-PBE) of the atomic species on the (6×6) (100), (4×6) (110) and (4×4) (111) surfaces of Na and Li. The reported DFT values were taken from our previous work.[85,86] For the calculated DFT-PBE values, the respective standard deviation calculated with BEEF-vdW[92] is given in parentheses. All values are reported in eV atom^{-1}.

		Sodium		Lithium	
	Adsorption side	ReaxFF	DFT-PBE	ReaxFF	DFT-PBE
(100)	bridge	-0.87	-0.81 (0.26)	-1.22	-1.23 (0.15)
	hollow	-0.98	-0.90 (0.26)	-1.31	-1.27 (0.15)
	ontop	-0.63	-0.59 (0.23)	-1.10	-1.07 (0.13)
(110)	hollow	-0.92	-0.81 (0.27)	-1.31	-1.34 (0.14)
	long-bridge	-0.93	-0.82 (0.25)	-1.32	-1.35 (0.13)
	short-bridge	-0.90	-0.79 (0.24)	-1.30	-1.35 (0.13)
	ontop	-0.87	-0.78 (0.25)	-1.37	-1.39 (0.14)
(111)	bridge	-0.92	-0.88 (0.26)	-1.39	-1.34 (0.15)
	fcc	-1.10	-1.11 (0.25)	-1.65	-1.61 (0.16)
	hcp	-0.94	-0.84 (0.26)	-1.19	-1.22 (0.15)
	ontop	-0.61	-0.51 (0.26)	-0.97	-0.90 (0.12)

Our parameterised potential function can reproduce the thermodynamic stability sequence of the adsorption sites on the respective surfaces for both metal systems. We also found an excellent agreement between the absolute adsorption energies generated with the optimised reactive force field and the DFT-PBE target values. The deviations between the pairs of values are well within the range of the computed standard deviation from DFT. Note that the adsorption properties of the bridge and ontop positions on Na(111) and Li(111) were correctly determined by ReaxFF without being included explicitly in the training routine.

Diffusion properties – We introduced selected self-diffusion pathways into the training routine to reflect the surface kinetics. For this purpose, characteristic processes along terraces, steps and kink structures on Na(100) and Li(100) were selected, and their respective diffusion barriers evaluated. Also, the symmetry of the images in the reaction profile of sym-

metrical processes was linked to the error function to reflect possible noise in the potential energy surface in the error value.

In this section, the self-diffusion processes on the low-index surfaces are showcased as an example. It should be noted that only the hopping and exchange processes on the (100) facets were included in the respective force field training. All other reaction pathways served to validate the quality and reliability of the obtained force field parameter set. An overview of the respective pathways can be found in Fig. 3. The respective ReaxFF activation energies and their DFT-PBE target values are summarised in Table 5.

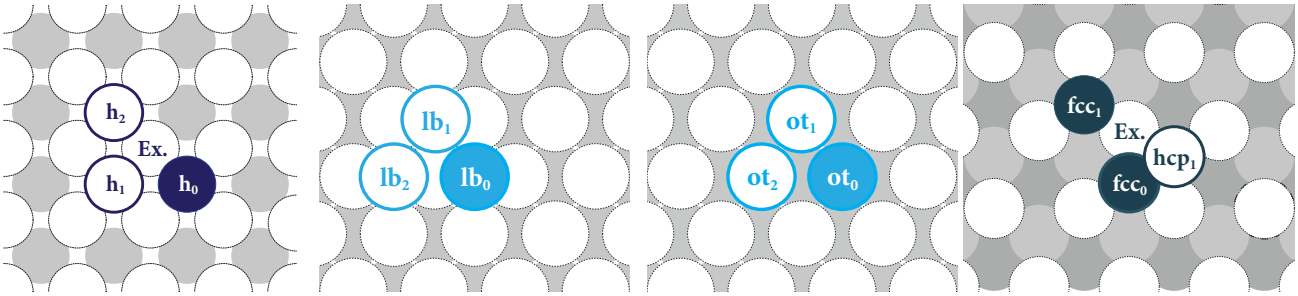

(a) (100) (b) Na(110) (c) Li(110) (d) (111)

Figure 3: Schematic representation of the studied self-diffusion processes on (a) Na(100) and Li(100), (b) Na(110), (c) Li(110), and (d) Na(111) and Li(111). The most stable adsorption site of the respective facet was set as the initial state, *i.e.* hollow (h), longbridge (lb), ontop (ot) and fcc. Here, a filled circle highlights the starting position, and a framed circle indicates possible end positions of the diffusion pathways. Atoms participating in the exchange process are marked with an Ex. label. The calculated forward and reversed activation energies are given in Table 5.

The obtained ReaxFF activation energies for the hopping processes ($h_0 \leftrightarrow h_1$, $h_0 \leftrightarrow h_2$) on Na(100) and Li(100) are marginally elevated compared to the DFT-PBE values but within the range of the calculated standard deviations. It was further possible to sufficiently describe the exchange process $h_0 \leftrightarrow h_2$ (Ex.) for Li, while for sodium, the process was overestimated by 70 meV. Increasing the weight of the process during the force field training led to a reduction of the barrier, but the overall description of Na got degraded. Applying the force field to the (110) surfaces of both metals, ReaxFF could reproduce the reverse stability order of the adsorption sites. The obtained activation energies for the respective diffusion pathways

Table 5: Calculated terrace self-diffusion barriers of sodium and lithium on its low-index surfaces by ReaxFF and DFT-PBE. For the calculated DFT-PBE values, the respective standard deviation calculated with BEEF-vdW[92] is given in parentheses. All forward (for) and reversed (rev) activation energies E_a are reported in eV.

			ReaxFF		DFT-PBE	
	(hkl)	Pathway	E_a^{for}	E_a^{rev}	E_a^{for}	E_a^{rev}
Sodium	(100)	$h_0 \leftrightarrow h_1$	0.12	0.12	0.09 (0.03)	0.09 (0.03)
		$h_0 \leftrightarrow h_2$	0.35	0.35	0.31 (0.09)	0.31 (0.09)
		$h_0 \leftrightarrow h_2$ (Ex.)	0.13	0.13	0.06 (0.03)	0.06 (0.03)
	(110)	$lb_0 \leftrightarrow lb_1$	0.04	0.04	0.04 (0.07)	0.04 (0.07)
		$lb_0 \leftrightarrow lb_2$	0.06	0.06	0.03 (0.04)	0.03 (0.04)
		$fcc_0 \leftrightarrow fcc_1$ (Ex.)	0.10	0.10	0.09 (0.04)	0.09 (0.04)
	(111)	$fcc_0 \leftrightarrow hcp_1$	0.20	0.03	0.27 (0.04)	0.00 (0.02)
		$fcc_1 \leftrightarrow hcp_1$ (Ex.)	0.30	0.13	0.29 (0.05)	0.03 (0.05)
Lithium	(100)	$h_0 \leftrightarrow h_1$	0.09	0.09	0.04 (0.04)	0.04 (0.04)
		$h_0 \leftrightarrow h_2$	0.21	0.21	0.20 (0.07)	0.20 (0.07)
		$h_0 \leftrightarrow h_2$ (Ex.)	0.14	0.14	0.11 (0.03)	0.11 (0.03)
	(110)	$ot_0 \leftrightarrow ot_1$	0.07	0.07	0.05 (0.03)	0.05 (0.03)
		$ot_0 \leftrightarrow ot_2$	0.05	0.05	0.05 (0.02)	0.05 (0.02)
		$fcc_0 \leftrightarrow fcc_1$ (Ex.)	0.09	0.09	0.13 (0.02)	0.13 (0.02)
	(111)	$fcc_0 \leftrightarrow hcp_1$	0.46	0.00	0.39 (0.07)	0.00 (—)
		$fcc_1 \leftrightarrow hcp_1$ (Ex.)	0.46	0.00	0.39 (0.07)	0.00 (—)

yielded an excellent agreement between ReaxFF and DFT-PBE. On Na(111) and Li(111), the exchange process $fcc_0 \leftrightarrow fcc_1$ (Ex.) was identified as the dominant diffusion mechanism. Our parameterised potential function correctly reproduces the priority order of the processes in both systems with the obtained parameter set. Apart from the preferred exchange process, the possible pathways on Li(111) from *fcc* to *hcp* are described within the error margin of DFT. For sodium, the forward activation barrier of $fcc_0 \leftrightarrow hcp_1$ is slightly underestimated. In contrast, the reverse diffusion barrier of the related exchange process ($fcc_1 \leftrightarrow hcp_1$ (Ex.)) was found to be 100 meV above the DFT-PBE target value.

6.2 Training and validation of Li-Na interaction

Alkali metal alloy anodes are considered possible candidates for the next-generation battery system beyond Li-ion batteries. Unlike bare alkali metal electrodes, the formation of den-

drites is prevented due to the electrostatic shield mechanism.[105,106] In a first study, Zhang *et al.* presented a dendrite-free metal-oxygen battery featuring a Li-Na alloy anode.[107] However, the electrochemistry of the alloy anode is still poorly understood and further studies in this area are required.[108]

For future studies on Li-Na alloys, we developed a parameter set for the description of Li-Na interactions in addition to the self-interactions of Na and Li. Analogous to metallic lithium and sodium, the bulk and surface properties of various Li-Na structures were investigated using DFT-PBE to generate a training set for the force field optimisation.

Bulk properties – The phase diagram for Li-Na systems shows a large immiscibility in the two metals' liquid and solid-state at standard conditions.[109] Instead, a eutectic alloy is formed where both alloy components maintain their crystal structures, and the alloy behaves neither as a solid solution nor as an intermetallic particle.[107] Hence, we generated different theoretical Li-Na alloy bulk phases with different compositions for the force field training of the Li-Na interaction to include a broad range of different binding structures. Apart from the lattice constants and angles, the bulk modulus of the respective phase was calculated by compressing and expanding the lattice. Further, the energy of formation per formula unit $\Delta_\mathrm{f}E$ referenced to the *bcc* bulk phases of lithium and sodium was determined by

$$\Delta_\mathrm{f}E = E_{\mathrm{Li}_x\mathrm{Na}_y} - x \cdot E_\mathrm{Li}^\mathrm{bulk} - y \cdot E_\mathrm{Na}^\mathrm{bulk} \ , \tag{46}$$

where $E_{\mathrm{Li}_x\mathrm{Na}_y}$ is the total binding energy of the $\mathrm{Li}_x\mathrm{Na}_y$ alloy phase, and $E_\mathrm{Li}^\mathrm{bulk}$, $E_\mathrm{Na}^\mathrm{bulk}$ are the cohesive energy of the Li and Na *bcc* bulk phase, respectively. Table 6 summarises the calculated structural and physical constants.

Our parameterised potential function correctly reproduces the lattice constants and angles of the respective phases. While the determined cell parameters of LiNa ($P\bar{6}m2$) and $\mathrm{Li_3Na}$ ($Cmcm$) match the DFT-PBE target values perfectly, we found a maximum deviation of 0.04 Å for the remaining bulk structures. As expected, all studied Li-Na alloy bulk structures yielded positive formation energies, indicating a thermodynamic instability relative to

Table 6: Calculated structural and physical constants for various bulk Li-Na alloy phases obtained from ReaxFF and DFT-PBE. The determined standard deviations obtained from BEEF-vdW[92] calculations are given in brackets. Lattice constants a_0, b_0, c_0 are given in Å, lattice angles α_0, β_0, γ_0 are given in °, energies of formation $\Delta_f E$ are given in eV, and bulk moduli B_0 are given in GPa. The energy of formation is reported per formula unit and is referenced to the *bcc* bulk phases of lithium and sodium (see Table 2).

	Space group		ReaxFF	DFT-PBE
LiNa	$Pm\bar{3}m$	a_0, b_0, c_0	3.82, 3.82, 3.82	3.85, 3.85, 3.85
		α_0, β_0, γ_0	90, 90, 90	90, 90, 90
		$\Delta_f E$	0.10	0.11 (0.02)
		B_0	11.5	10.2
LiNa	$P\bar{6}m2$	a_0, b_0, c_0	3.46, 3.46, 5.51	3.46, 3.46, 5.51
		α_0, β_0, γ_0	90, 90, 120	90, 90, 120
		$\Delta_f E$	0.13	0.11 (0.03)
		B_0	9.1	10.0
$LiNa_3$	$Pm\bar{3}m$	a_0, b_0, c_0	5.12, 5.12, 5.12	5.08, 5.08, 5.08
		α_0, β_0, γ_0	90, 90, 90	90, 90, 90
		$\Delta_f E$	0.20	0.15 (0.03)
		B_0	9.2	8.9
Li_3Na	$Cmcm$	a_0, b_0, c_0	6.50, 6.50, 5.34	6.50, 6.50, 5.34
		α_0, β_0, γ_0	90, 90, 120	90, 90, 120
		$\Delta_f E$	0.18	0.16 (0.03)
		B_0	11.4	11.6
Li_3Na	$I4/mmm$	a_0, b_0, c_0	4.58, 4.58, 4.58	4.60, 4.60, 4.60
		α_0, β_0, γ_0	90, 90, 90	90, 90, 90
		$\Delta_f E$	0.18	0.18 (0.03)
		B_0	13.3	11.7

their pure phases. Here, the differences in the $\Delta_f E$ values between ReaxFF and DFT-PBE are within the range of the DFT standard deviation, except for $LiNa_3$ which shows a significant discrepancy of 0.05 eV. The equation of state of the respective Li-Na alloy phases was also included in the reactive force field training. As shown by the resulting bulk moduli, the developed reactive force field can accurately reproduce the lattice expansion and compression. This allows an accurate description of phase transitions in reactive molecular dynamics simulations.

Diffusion properties – For further evaluation of the Li-Na parameter set, the diffusion of a single Na adatom on perfect and imperfect Li(100) surfaces was investigated. This

allows us to validate the description of both thermodynamically and kinetically controlled processes via the energy difference in the initial and final states and the computed activation energies, respectively. A schematic representation of the explored diffusion pathways is given in Fig. 4. The respective reversed and forward activation energies obtained from ReaxFF and DFT-PBE are listed in Table 7.

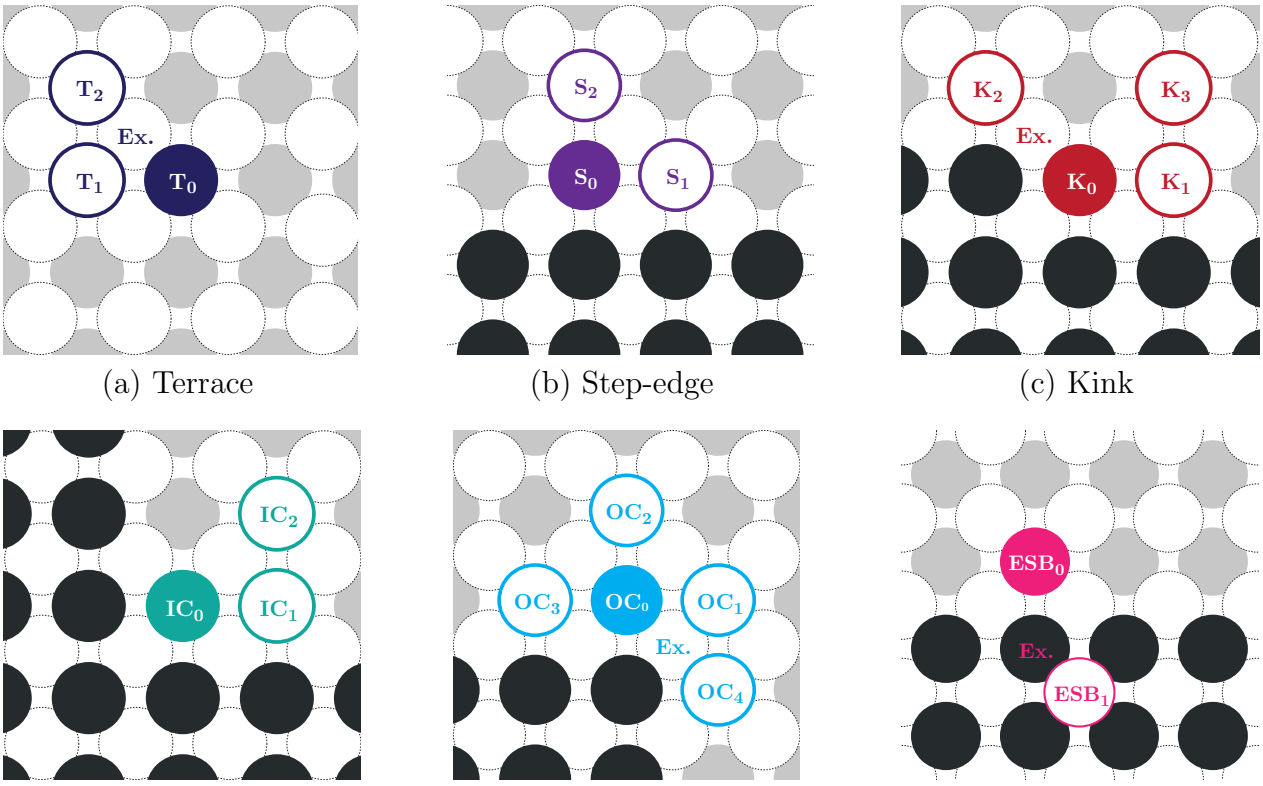

(a) Terrace (b) Step-edge (c) Kink

(d) Inner-corner (e) Outer-corner (f) ESB

Figure 4: Schematic representation of the studied diffusion processes of a single Na adatom on Li(100). A filled circle highlights the initial state, and a framed circle indicates possible final states of the diffusion pathways. Atoms participating in exchange processes are marked with an "Ex." label. The calculated forward and reversed activation energies are given in Table 7.

The terrace (T) diffusion barriers are in excellent agreement between ReaxFF and DFT-PBE. We found the hopping process $T_0 \leftrightarrow T_1$ with an activation energy of 0.05 eV (ReaxFF: 0.08 eV) to be the preferred diffusion pathway on the flat terrace structure. As expected, incorporating a Na atom into the Li(100) surface is highly unfavourable. Further, the bond of a single Na adatom at the preferred hollow side is weakened by 0.25 eV (ReaxFF: 0.20 eV)

Table 7: Calculated terrace diffusion barriers of a single Na adatom on Li(100) obtained by ReaxFF and DFT-PBE. All forward (for) and reversed (rev) activation energies E_a are reported in eV.

		ReaxFF		DFT-PBE	
System	Pathway	E_a^{for}	E_a^{rev}	E_a^{for}	E_a^{rev}
Terrace	$T_0 \leftrightarrow T_1$	0.08	0.08	0.05	0.05
	$T_0 \leftrightarrow T_2$	0.13	0.13	0.13	0.13
	$T_0 \leftrightarrow T_2$ (Ex.)	0.25	0.12	0.26	0.09
Step-edge	$S_0 \leftrightarrow S_1$	0.06	0.06	0.06	0.06
	$S_0 \leftrightarrow S_2$	0.17	0.06	0.18	0.02
Kink	$K_0 \leftrightarrow K_1$	0.12	0.05	0.14	0.04
	$K_1 \leftrightarrow K_3$	0.18	0.07	0.22	0.04
	$K_0 \leftrightarrow K_4$ (Ex.)	0.33	0.06	0.37	0.04
Inner-corner	$IC_0 \leftrightarrow IC_1$	0.14	0.04	0.16	0.03
	$IC_1 \leftrightarrow IC_2$	0.17	0.07	0.21	0.03
Outer-corner	$OC_0 \leftrightarrow OC_1$	0.13	0.03	0.17	0.02
	$OC_0 \leftrightarrow OC_2$	0.16	0.06	0.17	0.02
	$OC_0 \leftrightarrow OC_3$	0.04	0.06	0.03	0.06
	$OC_0 \leftrightarrow OC_4$ (Ex.)	0.25	0.07	0.25	0.06
ESB	$ESB_0 \leftrightarrow ESB_1$	0.28	0.15	0.32	0.16
	$ESB_0 \leftrightarrow ESB_1$ (Ex.)	0.38	0.11	0.42	0.17

compared to the adsorption of a Li atom on Li(100). The diffusion barrier for the migration via the ontop position ($T_0 \leftrightarrow T_2$) into the adjacent hollow side is slightly reduced relative to the identical self-diffusion process.

For the step-edge (S) structures, the developed reactive force field can adequately recreate the different diffusion processes. Here, hardly any activation barrier was found for the diffusing Na adatom along the step-edge ($S_0 \leftrightarrow S_1$). Its activation energy of 0.06 eV (ReaxFF: 0.06 eV) has the same order of magnitude as the favoured terrace hopping mechanism $T_0 \leftrightarrow T_1$. Also, the attachment process $S_2 \rightarrow S_0$ towards the step-edge is highly preferred over its inverse counterpart $S_0 \rightarrow S_2$. While an energy barrier of 0.18 eV (ReaxFF: 0.17 eV) hinders the detachment of the Na atom, the inverse attachment process is almost barrier-free (DFT-PBE: E_a= 0.02 eV, ReaxFF: E_a= 0.06 eV).

Subsequently, we analysed surface structures featuring corners and kinks, *i.e.* kink-sites (K), inner-corners (IC), outer-corners (OC). For these diffusion pathways, the determined ReaxFF activation energies show only marginal deviations of less than 0.05 eV versus the DFT-PBE target values. The perpendicular detachment of a Na adatom onto the flat terrace ($K_1 \rightarrow K_3$, $IC_1 \rightarrow IC_2$, $OC_0 \rightarrow OC_2$) exhibited a diffusion barrier of $0.17 - 0.22$ eV (ReaxFF: $0.16 - 0.18$ eV) in all three systems and is highly unfavourable to their inverse processes ($K_3 \rightarrow K_1$, $IC_2 \rightarrow IC_1$, $OC_2 \rightarrow OC_0$). Increasing the number of immediate neighbours leads to a thermodynamically stabilised state. Here, the incorporation of the Na atom into inner-corners and kink-sites ($IC_1 \rightarrow IC_0$, $K_1 \rightarrow K_0$) is hardly hindered by activation barriers of less than 0.05 eV (ReaxFF: 0.06 eV). At outer corners, the migration along the step-edge ($OC_0 \rightarrow OC_3$) is favoured to the vertical detachment process $OC_0 \rightarrow OC_2$ and the atom's translation around the corner ($OC_0 \rightarrow OC_4$ and $OC_0 \rightarrow OC_4$ (Ex.)). Unlike Li self-diffusion, the barrier for shifting atoms around the corner via the exchange mechanism $OC_0 \rightarrow OC_4$ (Ex.) is more than twice as high (DFT: 0.25 eV *vs* 0.11 eV, ReaxFF: 0.25 eV *vs* 0.14 eV) due to the extensive immiscibility of both metals.

Besides the two-dimensional intralayer mass transport, we have also studied the interlayer mass transport across step-edges. An additional energy barrier E_{ES}, also known as the Ehrlich-Schwöbel barrier (ESB), must be exceeded while crossing the step-edge. The additional energy contribution results from the under-coordination of the diffusing species during the step-down migration. Here, the step-down diffusion via atom hopping ($ESB_0 \leftrightarrow ESB_1$) and the push-out mechanism ($ESB_0 \leftrightarrow ESB_1$ (Ex.)) were examined. Our parameterised potential function is capable of correctly reproducing the energetic sequence of the activation energies. Only minor differences of up to 0.06 eV have been observed between the computed values from ReaxFF and DFT-PBE. Our study showed that the hopping process $ESB_0 \rightarrow ESB_1$ is preferred to the incorporation of the Na atom into the step-edge via $ESB_0 \rightarrow ESB_1$ (Ex.). Due to the higher atomic coordinates, the initial state ESB_0 is thermodynamically more stable than the final state ESB_1 on the upper terrasse.

6.3 Grand Canonical Monte Carlo

The GCMC approach[110,111] is a stochastic method for studying the thermodynamic equilibrium structures at a given chemical potential μ. A series of Monte Carlo trial moves are carried out by the GCMC algorithm and accepted or rejected based on the minimum energy of the trial geometry. Each trial movement entails either the addition (insert), removal (remove) or displacement (move) of a particle. The Boltzmann probabilities P for accepting the respective MC steps are calculated by

$$P_{\text{insert}}^{\text{accept}} = \min\left[1, \frac{V_{\text{acc}}}{\Lambda^3(N+1)} \exp\left(-\frac{E_{\text{new}} - E_{\text{old}} - \mu_{\text{res}}}{k_{\text{B}}T}\right)\right] , \tag{47}$$

$$P_{\text{remove}}^{\text{accept}} = \min\left[1, \frac{N\Lambda^3}{V_{\text{acc}}} \exp\left(-\frac{E_{\text{new}} - E_{\text{old}} + \mu_{\text{res}}}{k_{\text{B}}T}\right)\right] , \tag{48}$$

$$P_{\text{move}}^{\text{accept}} = \min\left[1, \exp\left(-\frac{E_{\text{new}} - E_{\text{old}}}{k_{\text{B}}T}\right)\right] , \tag{49}$$

where Λ is the thermal de Broglie wavelength of the exchanged particle, N is the number of the system's exchangeable particles before the MC move, $E_{\text{new}} - E_{\text{old}}$ is the total energy difference before (old) and after (new) the MC move, and μ_{res} is the chemical potential of the particle reservoir.[110] From the difference between the total volume V and the occupied volume V_{occ}, the accessible volume V_{acc} is determined following

$$V_{\text{acc}} = V - V_{\text{occ}} = V - N\frac{4}{3}\pi r^3 , \tag{50}$$

where r is the atomic radius of the given species. The Monte Carlo (MC) algorithm accepts steps resulting in decreased system energy and moves that increase the energy with a certain probability. All steps are repeated in an iterative procedure until an appropriate termination criterion is met.

6.3.1 Li and Na nanoparticles

The thermodynamically driven surface growth on Li and Na was examined in the framework of a coupled ReaxFF/GCMC approach. To determine the minimum energy of the respective structures, we adopted the developed and validated ReaxFF force field potential for Li and Na. Different nanoparticle shapes (∼1000 atoms) were used as an initial structure for the GCMC simulation to consider the influence of the various crystal facets and edges. The equilibrium shape of the particles was generated from a potential-dependent Wulff construction. Particle shapes were generated for reductive conditions ($E = -1.50$ V/Li and $E = -1.00$ V/Na), neutral conditions ($E^0_{\mathrm{Li^+/Li}} = \pm 0.0$ V/Li and $E^0_{\mathrm{Na^+/Na}} = \pm 0.00$ V/Na), and oxidative conditions ($E^{\mathrm{PZC}}_{\mathrm{Li}} = +1.53$ V/Li and $E^{\mathrm{PZC}}_{\mathrm{Na}} = +0.94$ V/Na). We derived the required surface energy values for a given electrode potential E from Lippmann's electrocapillary curves[112] following

$$\gamma_{hkl}(E) = \frac{-C^{\mathrm{s}}_{hkl}}{2}\left(E - E^{\mathrm{PZC}}_{hkl}\right)^2 + \gamma^{\mathrm{PZC}}_{hkl}\ , \tag{51}$$

where C^{s}_{hkl} is the surface capacitance, E^{PZC}_{hkl} is the potential of zero charge (PZC), and $\gamma^{\mathrm{PZC}}_{hkl}$ is the surface tension at zero-charge of a (hkl) surface. The needed quantities can be obtained from potential-dependent grand canonical DFT calculations and were adopted from Hagopian *et al.*[113] An overview of the used data set and the obtained nanoparticle shapes are given in Table 8 and Fig. 5, respectively.

The equilibrium shape of the zero-charged Na-particle ($E^{\mathrm{PZC}}_{\mathrm{Na}}$) is composed of eight surfaces, *i.e.* {100} (14.5 %), {110} (45.9 %), {210} (9.8 %), {310} (1.8 %), {311} (0.5 %), {320} (8.2 %), {321} (18.8 %), and {332} (0.5 %). Similarly, the Li-particle at the potential of zero-charge ($E^{\mathrm{PZC}}_{\mathrm{Li}}$) is formed by {100} (21.7 %), {110} (14.8 %), {111} (3.0 %), {210} (19.9 %), {221} (16.1 %), {311} (5.0 %), {320} (18.7 %), and {332} (0.8 %) planes. At the redox-pair potential of Na ($E^0_{\mathrm{Na^+/Na}}$) and Li ($E^0_{\mathrm{Li^+/Li}}$), the resulting nanoparticle is restricted to {100} (Na: 13.3 %, Li: 25.2 %) and {110} (Na: 86.7 %, Li: 74.8 %) facets. For both metals, a

Table 8: Theoretical surface energy values $\gamma_{hkl}^{\mathrm{PZC}}$, potential of zero charge (PZC) values E_{hkl}^{PZC}, and surface capacitance values C_{hkl}^{s} for different (hkl) surfaces of sodium and lithium. All values have been adapted from Hagopian *et al.*[113] The values for E_{hkl}^{PZC}, $\gamma_{hkl}^{\mathrm{PZC}}$, and C_{hkl}^{s} are given in V per Na and Li, $\mathrm{J\,m^{-2}}$, and $\mu\mathrm{F\,cm^{-2}}$, respectively.

	Sodium			Lithium		
(hkl)	E_{hkl}^{PZC}	$\gamma_{hkl}^{\mathrm{PZC}}$	C_{hkl}^{s}	E_{hkl}^{PZC}	$\gamma_{hkl}^{\mathrm{PZC}}$	C_{hkl}^{s}
(100)	0.87	0.220	7.56	1.53	0.466	7.50
(110)	1.03	0.211	7.46	1.67	0.492	8.46
(111)	0.78	0.250	7.79	1.24	0.526	7.46
(210)	0.91	0.225	7.24	1.47	0.494	7.66
(211)	0.91	0.238	7.37	1.53	0.535	7.62
(221)	0.88	0.241	7.27	1.25	0.520	7.72
(310)	0.88	0.229	7.53	1.50	0.499	7.34
(311)	0.86	0.238	7.21	1.43	0.520	6.73
(320)	0.95	0.221	7.02	1.49	0.493	7.14
(321)	0.93	0.231	7.53	1.47	0.529	7.91
(322)	0.86	0.244	7.18	1.35	0.536	6.79
(331)	0.91	0.234	7.02	1.26	0.520	7.14
(332)	0.83	0.244	7.53	1.26	0.526	7.40

rhombic dodecahedron consisting of {110} surfaces is found at reductive conditions.

The individual particles were used as an initial structure for the ReaxFF/GCMC calculation. For the investigation of the surface growth, a chemical potential equivalent to the cohesive energy of the respective metal at 300 K was assumed. A radial distribution function (RDF) is used to describe the distance-dependent distribution of the atomic species on the particle. For this purpose, the distances between the system's atom pairs are computed and represented as a volume-normalised density. Fig. 6 shows the radial distribution functions obtained for the different Na- and Li-particles.

A comparable peak distribution can be found for the radial distribution functions of the initial zero-charged nanoparticles and the equilibrium structure at the respective redox pair potential. Both systems show a similar shape and are dominated by {100} and {110} planes. Deviations can be observed for the rhombic dodecahedron, which is entirely composed of {110} facets.

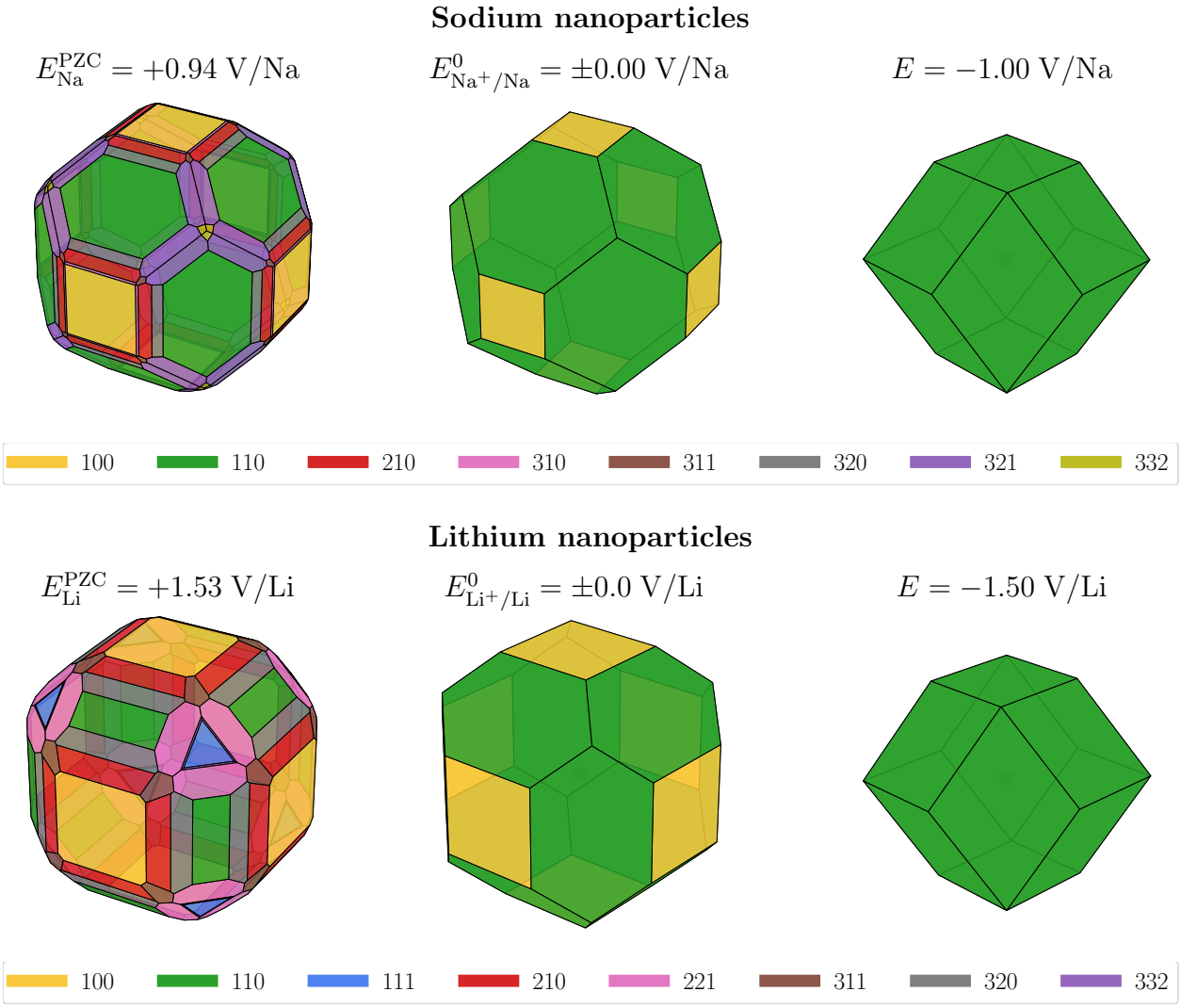

Figure 5: Schematic representation of the different Li and Na nanoparticles. The particles were generated using a potential-dependent Wulff construction for different electrode potentials, *i.e.* $E = -1.50$ V/Li and $E = -1.00$ V/Na (reductive condition), $E^{0}_{Li/Li^+} = \pm 0.0$ V/Li and $E^{0}_{Na/Na^+} = \pm 0.00$ V/Na, and $E^{PZC}_{Li} = +1.53$ V/Li and $E^{PZC}_{Na} = +0.94$ V/Na (oxidative conditions). The potential-dependent surface energies for the Wulff approach were derived from the grand-canonical DFT calculations of Hagopian *et al.*[113]

In the GCMC simulation, metal atoms were successively introduced into the respective systems. Thereby, a homogeneous surface growth on the individual nanoparticles was observed. For both metals, the formation of {100} surface facets on the rhombic dodecahedron particles occurs. After the deposition of 4080 atoms on the respective particles of sodium and lithium, we obtained nearly identical RDFs for the studied equilibrium structures. The sharp peaks

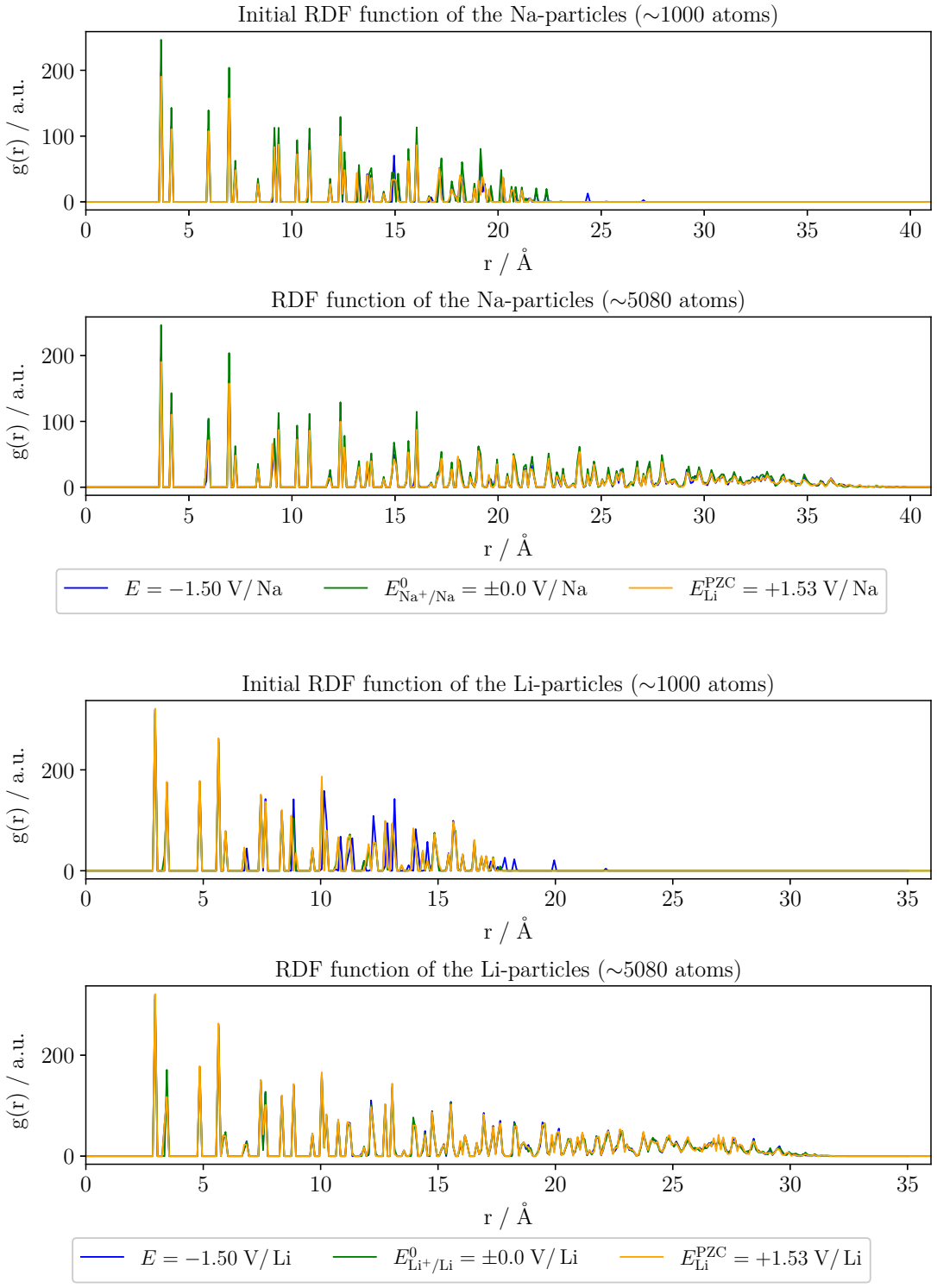

Figure 6: Radial distribution functions (RDFs) for the different Li and Na nanoparticles of the initial GCMC structures (∼1000 atoms) and after the deposition of ∼4080 metal atoms. The entries in the legend refer to the different particle shapes, as shown in Fig. 5.

indicate a long-range ordering of the atoms and thus a crystalline structure of the particle. In the outer region, some diffuse peaks are present, which can be explained by the stochastic nature of the GCMC approach.

6.4 Kinetic Monte Carlo

Finally, the initial growth processes on Li(100) and Na(100) are investigated utilising kMC simulations within the developed multi-scale model. kMC is a stochastic method for large-scale simulations to describe the evolution of a system over time. The system's dynamics are described by hops on the potential energy surface from one local minimum to a neighbouring one. In this process, the previously developed and validated reactive force field potential is used to generate the required rate catalogue. The latter provides the activation energies E_a and pre-exponential factors k_0 to determine the reaction rates of viable diffusion processes. For a diffusion process i, its reaction rate k_i is determined following

$$k_i = k_{0,i} \exp\left(-\frac{E_{\mathrm{a},i}}{k_\mathrm{B}T}\right) , \tag{52}$$

where T is the temperature, and k_B is the Boltzmann constant. The pre-exponential factor $k_{0,i}$ is estimated based on the harmonic transition state theory from the vibration modes at the initial state (IS) and transition state (IS) of process i. This assumption is only valid as long as the IS does not differ much from the TS. Due to the substantial entropy reduction at the deposition of a species from the gas phase onto a metal surface, the reaction rate for non-activated adsorption processes k_ad is more accurately calculated by

$$k^\mathrm{ad}_{\mathrm{n,B}}(T,p) = \tilde{S}_{n,B}(T)\frac{p_n A_\mathrm{uc}}{\sqrt{2\pi m_n k_\mathrm{B}T}} , \tag{53}$$

where $\tilde{S}_{n,B}(T)$ is the temperature-dependent sticking coefficient of site B, p_i is the partial pressure of species n of mass m, and A_uc is the surface unit cell area.[114,115] The rate constant k^des_n for the reverse desorption process of a species n from the surface becomes

$$k_n^{\mathrm{des}} = \frac{k_{\mathrm{B}}T}{h} \exp\left(-\frac{E_{\mathrm{a},n}}{k_{\mathrm{B}}T}\right) \ , \tag{54}$$

where h is the Planck constant. In each iteration of the kMC simulation, the calculated reaction rates k_i for the respective diffusion, adsorption and desorption events are summed up to a total reaction rate k_{tot}, as follows:

$$k_{\mathrm{tot}} = \sum_{i=1}^{N} k_i \ . \tag{55}$$

Based on the random numbers $\rho_1 \in [0,1]$, the process q, which meets the condition $\sum_{i=1}^{q-1} k_i \geq \rho_1 k_{\mathrm{tot}} \geq \sum_{i=1}^{q} k_i$, is then extracted and executed. The average escape time of the selected process is computed based on the random number $\rho_2 \in (0,1]$ and the total reaction rate k_{tot} to propagate the system time t following

$$t \rightarrow t - \frac{1}{k_{\mathrm{tot}}} \ln\left(\rho_2\right) \ . \tag{56}$$

Subsequently, all possible reaction events for the new system configuration are identified to repeat steps (52) - (56) in an iterative manner until a termination criterion is met.

6.4.1 Diffusion events and lattice construction

Our previous first principles studies[85,86] showed that both hopping and exchange processes need to be considered for a comprehensive description of the diffusion events for Li and Na surface systems. The analysis of the dimer interaction energies showed an attractive interaction of the nearest neighbours (NN) with the diffusing adatom but a negligible impact of the next-nearest neighbours. Here, we have adopted a lattice gas approach to describe the diffusion events within our in-house kMC implementation. Each grid point is defined by the translation vector T, following

$$\mathbf{T} = m \cdot \mathbf{x}_1 + n \cdot \mathbf{x}_2 \ , \quad m,n \in \mathbb{N}_0^+ \ , \tag{57}$$

where $\mathbf{x}_1 = x(a_0, 0)$ and $\mathbf{x}_2 = x(0, a_0)$. In the description of the diffusion processes, the NN are taken into account. The resulting mesh structures for the respective diffusion mechanisms are given in Fig. 7.

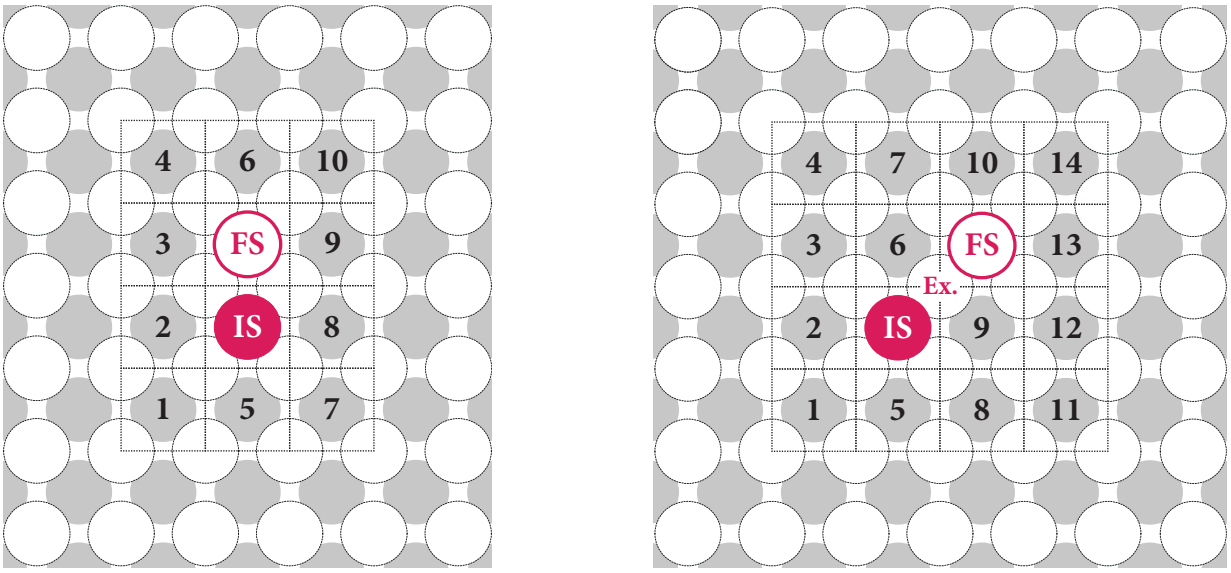

(a) hopping (b) exchange

Figure 7: Schematic representation of the chosen kinetic Monte Carlo lattice for (a) hopping and (b) exchange processes on Li(100) and Na(100). The initial state (IS) and final state (FS) highlight the initial and final position of the diffusion pathway, respectively. Atoms participating in exchange processes are marked with an Ex. label. The neighbour positions 1-10 (hopping) and 1-14 (exchange) can either be empty or occupied and define the surface structure of the diffusion process.

Nudged Elastic Band calculations were carried out using the developed reactive force field potential to determine the respective activation energies. From the vibration modes ν_i of the initial and transition state, the pre-exponential factor k_0 was obtained following

$$k_0 = \frac{\prod_i^{3N} \nu_i^{\mathrm{IS}}}{\prod_i^{3N-1} \nu_i^{\mathrm{TS}}} \,. \tag{58}$$

All ReaxFF calculations were performed on an eight-layer 10x10 (100) slab, where the two lowermost layers have been kept in their bulk structure. The entire outgoing row of atoms was occupied for each occupied surrounding site when generating the surface structure. In

total, $2^{10} = 1024$ hopping and $2^{14} = 16384$ exchange processes are included in our kMC simulation.

6.4.2 Nucleation and Aggregation

First, adatoms were randomly distributed on the 100×100 (100) surface at different surface coverages (*i.e.* 0.5 ML, 0.25 ML, 0.125 ML, and 0.0625 ML) to study nucleation and aggregation processes on metallic sodium and lithium. All systems were evaluated at 100 K, 200 K, 300 K, and 400 K, respectively. Snapshots from the kMC simulation of the initial growth and aggregation processes for both metals are given in Fig. 8.

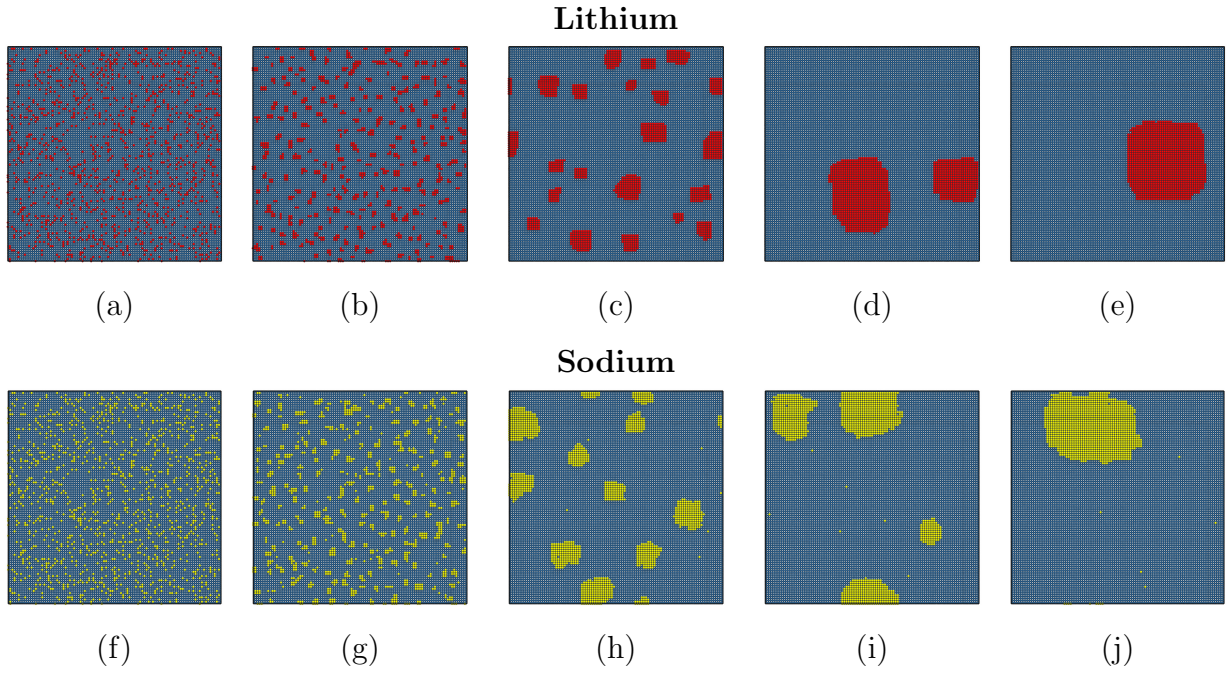

Figure 8: Snapshots of the initial nucleation and aggregation processes on 100×100 Li(100) (red, (a)-(e)) and 100×100 Na(100) (yellow, (f)-(j)) at 200 K and a surface coverage of 0.125 ML. The initial configuration was generated by a random distribution of adatoms on the respective surface. Hopping and exchange processes were considered for both systems, and the number of adatoms was kept fixed during the simulation. (a) Initial structure, (b) after 2.0×10^{-7} s, (c) 1.7×10^{-4} s, (d) 3.1 s, (e) 2.5×10^{1} s, (f) initial structure, (g) after 4.1×10^{-7} s, (h) 3.8×10^{-3} s, (i) 3.8×10^{-2} s, (j) 1.8 s.

Initially, nucleation seeds are formed on the surface of both metals after a few nanoseconds. These nuclei gradually form small islands and keep growing continuously. Aggregation

of islands is observed until only one individual round-shaped island remains on the surface after a few seconds. The nucleation processes occur within a few nanoseconds at all investigated temperatures due to the low terraced diffusion barrier; however, the growth rate of the islands is highly temperature-dependent. While terrace self-diffusion and migration along step-edges are almost barrier-free on both surfaces,[85,86] the detachment barrier of an adatom perpendicular to the step is hindered by increased activation energies. Any temperature increase improves the probability of processes with higher diffusion barriers.

6.4.3 Diffusion coefficients

The mean square displacement (MSD) of the respective adatoms was tracked throughout the simulations to characterise the diffusion and growth processes. Taking the obtained MSD, the system's diffusion constant D can then be calculated as

$$D = \frac{\langle \mathrm{MSD}(t) - \mathrm{MSD}_0 \rangle}{2dt} \,, \tag{59}$$

where t is the simulation time, and d is the lattice dimension ($d = 2$ in this case). The diffusion coefficient measures the mobility of the particles in a system and is an essential parameter for simulations on larger scales. An overview of the calculated diffusion constants and the average mean square displacement for different surface coverages is given in Table 9 and Fig. 9, respectively.

As expected, low temperatures and increased surface coverage reduce the adatom mobility on the surfaces. At 100 K, migration along step-edges is the primary diffusion process, accounting for up to 52 % (Li) and 76 % (Na) of all diffusion events. In general, the resulting diffusion constants for sodium are two orders of magnitude higher than those for lithium. While the exchange mechanism is almost non-existent for Li at this temperature, about 10 % of the diffusion events on Na(100) occur via an exchange process. Here, the main events are migrations of the adatom around outer-corners and kink sites. These differences are also

Table 9: Calculated average diffusion coefficient for adatoms on Li(100) and Na(100) for different surface coverages Θ. All values are reported in $m^2\,s^{-1}$.

	Θ	100 K	200 K	300 K
Lithium	1/2 ML	$(1.6 \pm 0.8) \times 10^{-21}$	$(4.4 \pm 0.4) \times 10^{-15}$	$(6.5 \pm 2.8) \times 10^{-13}$
	1/2 ML (hop.)	$(1.7 \pm 0.2) \times 10^{-21}$	$(1.0 \pm 0.3) \times 10^{-15}$	$(2.2 \pm 1.2) \times 10^{-13}$
	1/4 ML	$(6.8 \pm 1.3) \times 10^{-21}$	$(6.1 \pm 0.2) \times 10^{-15}$	$(2.5 \pm 0.1) \times 10^{-12}$
	1/4 ML (hop.)	$(6.4 \pm 0.6) \times 10^{-21}$	$(3.7 \pm 0.3) \times 10^{-15}$	$(1.5 \pm 0.0) \times 10^{-12}$
	1/8 ML	$(1.4 \pm 0.4) \times 10^{-20}$	$(1.0 \pm 0.0) \times 10^{-14}$	$(5.1 \pm 0.2) \times 10^{-12}$
	1/8 ML (hop.)	$(2.1 \pm 0.4) \times 10^{-20}$	$(8.2 \pm 0.5) \times 10^{-15}$	$(3.8 \pm 0.1) \times 10^{-12}$
	1/16 ML	$(1.7 \pm 0.8) \times 10^{-20}$	$(1.9 \pm 0.1) \times 10^{-14}$	$(1.1 \pm 0.0) \times 10^{-11}$
	1/16 ML (hop.)	$(7.0 \pm 2.6) \times 10^{-20}$	$(1.9 \pm 0.1) \times 10^{-14}$	$(8.7 \pm 0.4) \times 10^{-12}$
Sodium	1/2 ML	$(8.8 \pm 8.3) \times 10^{-19}$	$(9.3 \pm 2.3) \times 10^{-14}$	$(1.0 \pm 0.1) \times 10^{-11}$
	1/2 ML (hop.)	$(5.9 \pm 0.7) \times 10^{-19}$	$(1.8 \pm 0.4) \times 10^{-14}$	$(1.9 \pm 0.2) \times 10^{-12}$
	1/4 ML	$(5.4 \pm 1.3) \times 10^{-19}$	$(2.1 \pm 0.1) \times 10^{-13}$	$(2.8 \pm 0.0) \times 10^{-11}$
	1/4 ML (hop.)	$(1.3 \pm 0.2) \times 10^{-18}$	$(3.3 \pm 0.4) \times 10^{-14}$	$(4.8 \pm 0.3) \times 10^{-12}$
	1/8 ML	$(4.6 \pm 2.0) \times 10^{-19}$	$(3.7 \pm 0.1) \times 10^{-13}$	$(6.0 \pm 0.2) \times 10^{-11}$
	1/8 ML (hop.)	$(1.8 \pm 0.3) \times 10^{-18}$	$(5.2 \pm 0.4) \times 10^{-14}$	$(1.0 \pm 0.0) \times 10^{-11}$
	1/16 ML	$(3.1 \pm 1.5) \times 10^{-19}$	$(6.9 \pm 0.3) \times 10^{-13}$	$(1.2 \pm 0.1) \times 10^{-10}$
	1/16 ML (hop.)	$(1.7 \pm 0.3) \times 10^{-18}$	$(9.7 \pm 0.8) \times 10^{-14}$	$(2.2 \pm 0.1) \times 10^{-11}$

evident in the diffusion constants obtained for simulations with and without an exchange process (see Table 9). By taking exchange mechanisms into account, higher mobility of the adatoms can be observed.

At 200 K, the fraction of terrace diffusion rises to 42 % (Na) and 36 % (Li). The higher temperature facilitates overcoming the kinetic hindrance of detachment processes from individual adatoms onto the terrace. In this way, individual atoms can be interchanged more frequently via the terrace between the island structures, leading to accelerated island growth. Additionally, the share of exchange processes increases up to 10 % and 48 % on Li(100) and Na(100), respectively. In both metal systems, the exchange mechanism is the preferred process for crossing corner structures, enabling the island to reach its equilibrium shape more swiftly. Smaller surface structures can move across the surface via exchange processes and aggregate to larger islands. When comparing the diffusion constants of simulations with and without exchange processes, differences of up to one order of magnitude can be found.

The significance of the exchange mechanism is also evident in Fig. 9. For the same surface

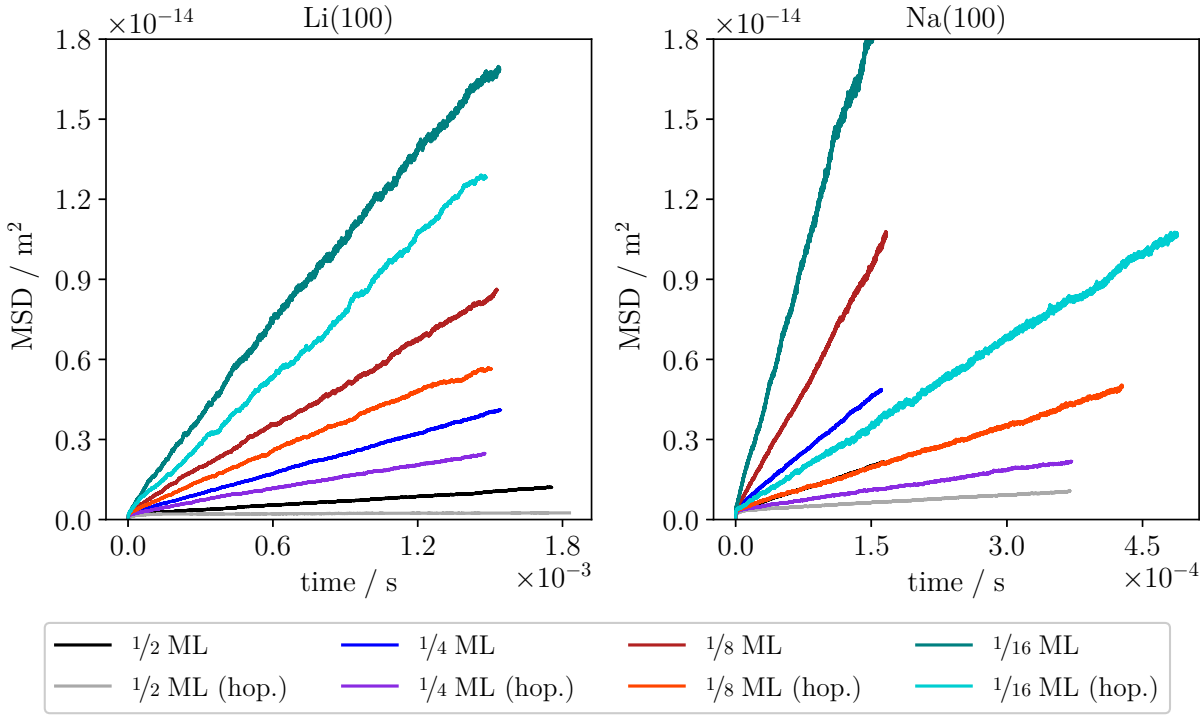

Figure 9: Averaged mean square displacements of adatoms for different surface coverages (*i.e.* 0.5 ML, 0.25 ML, 0.125 ML, and 0.0625 ML) on Li(100) (left) and Na(100) (right) at 300 K. For entries labelled with "(hop.)", only hopping processes were considered during the kMC simulation. In the case of Na(100), the graph of "1/2 ML" is overlapped by "1/8 ML (hop.)". The corresponding diffusion coefficients are given in Table 9.

coverage at 300 K, the MSD grows significantly faster. Here, according to Eq. (59), the graph's slope represents the system's diffusion coefficient. The impact is even more apparent for Na than for Li due to the higher proportion of ongoing exchange processes.

7 Conclusions

In this work, we have developed an improved approach to parameterise reactive force fields for solid-state systems using evolutionary algorithms together with an extended training routine.

First, different force-based optimisers with constraints, transition state tools, and frequency analysis were implemented in the stand-alone ReaxFF framework of the Amsterdam Model-

ing Suite (2018 and later). The introduced methods facilitate the adoption of the obtained DFT structures and are needed for the extended training routine.

Within the developed *KVIK* optimisation framework, we provide multiple evolutionary algorithms for the force field optimisation, *i.e.* PSO, CPSO, DE, CMA-ES, and VD-CMA. In a benchmark study on mathematical test functions, the performance of the different optimisers was evaluated and compared with the standard SOPPI procedure. The CPSO proved to be highly robust and showed superior performance over the standard PSO approach due to an enhanced diversity of the swarm. While the DE algorithm generally converges reliably and rather quickly to the global solution, a careful selection of the differential evolution strategy is needed. The Covariance Matrix Adaptation approaches find a strongly improved result after only a few optimisation iterations; however, premature convergence has been observed for highly complex benchmark functions such as *Schwefel* or *Xin-She Yang N.4*.

SOPPI proved to be an efficient optimisation approach with fast convergence within only a few iterations but had a strong tendency to get trapped in a local minimum for multimodal functions. Thereby, the optimisation performance was susceptible to the selected step length. In optimising reactive force fields with the SOPPI approach, a deeper understanding of the respective parameters and their optimisation range is required. However, it enables the user to gradually follow and retrace the optimisation process and thus facilitates the re-optimisation of the parameter set.

In contrast, evolutionary algorithms feature excellent exploration capabilities within the model parameter space and can be parallelised readily with near-linear scaling. These algorithms demonstrate their robustness in finding good fitting solutions in sampling search spaces of varying complexity and dimensionality. Also, the concurrent fitting of parameters provides an enhanced mapping of the existing parameter correlations. The extensive sampling of the model parameter space minimises the risk of getting caught in a local minimum and limits the influence of the parameter set's initial guess on the optimisation performance. Next, we developed an advanced training routine for the optimisation of solid-state systems.

The system's respective bulk phases are initially explored using the given parameter set, and their individual lattice constants, cohesive energies, and bulk moduli are calculated. All further structures of the training set are adjusted on the fly according to the determined minimum lattice constant to prevent distortion of the error value through possible lattice strain effects. Similar to the classical training set, surface and adsorption energies are evaluated, and their values are compared to the weighted reference data. Well-selected diffusion processes on perfect and imperfect surfaces were considered in the training routine to accurately describe the potential energy surface and the surface kinetics through the ReaxFF potential. The corresponding MEP and activation barriers were obtained from the implemented NEB method. Finally, the vibration modes of the initial, transition and final states were computed, and the resulting frequencies and pre-exponential factors were evaluated versus the reference data set.

We then used the developed *KVIK* optimisation framework to train a reactive force field potential to describe the Li-Li, Na-Na and Li-Na interactions. The obtained ReaxFF parameter set can reproduce both systems' bulk and surface properties almost entirely within the margin of the calculated DFT standard deviation. We demonstrated that our proposed optimisation approach enables an efficient and accurate way to train reactive force field potentials in an automated fashion.

Finally, MC simulations were performed to study the initial surface growth phenomena on metallic Li- and Na surfaces. The thermodynamically driven growth on different Li- and Na-particles was investigated using a coupled ReaxFF/GCMC approach. Homogeneous surface growth was observed during the deposition of the respective metallic species on the particle structures. An analysis of the RDF indicated a crystalline, long-range order of the system's atoms.

Subsequently, we have studied the influence of surface kinetics on the metals growth behaviour using a ReaxFF/kMC approach. The required activation energies and pre-exponential factors were computed utilising the developed ReaxFF potential and the implemented tran-

sition state tools. In the process, the nucleation and aggregation processes on Li(100) and Na(100) were analysed. By tracking the mean square displacement of the individual adatoms, we obtained the temperature and surface coverage dependent average diffusion coefficients. This study further demonstrated the importance of considering the exchange mechanism to describe growth processes on metallic Na and Li surfaces adequately.

Acknowledgement

This research was conducted as part of the German Research Foundation (DFG) under Project ID 390874152 (POLiS Cluster of Excellence) as well as the Sonderforschungsbereiche (collaborative research centers) SFB-1316 and SFB-1249. In addition, support from the BMBF (Bundesministerium für Bildung und Forschung) through the project InnoSüd (Grant Agreement: 03IHS024D) is gratefully acknowledged. Further, the authors acknowledge the computer time supported by the state of Baden-Württemberg through the bwHPC project and the DFG through grant number INST40/467-1 FUGG.

Supporting Information Available

Detailed information on the implemented transition state tools for ReaxFF, extended benchmark study results, reactive force field parameters for Li-Li, Na-Na, Li-Na, and Mg-Mg, and their comparison with literature known ReaxFF parameter sets are given in the supplementary material.

References

(1) van Duin, A. C. T.; Dasgupta, S.; Lorant, F.; Goddard, W. A. ReaxFF: A Reactive Force Field for Hydrocarbons. *The Journal of Physical Chemistry A* **2001**, *105*, 9396–9409.

(2) Chenoweth, K.; van Duin, A. C. T.; Goddard, W. A. ReaxFF Reactive Force Field for Molecular Dynamics Simulations of Hydrocarbon Oxidation. *The Journal of Physical Chemistry A* **2008**, *112*, 1040–1053.

(3) Senftle, T. P.; Hong, S.; Islam, M. M.; Kylasa, S. B.; Zheng, Y.; Shin, Y. K.; Junkermeier, C.; Engel-Herbert, R.; Janik, M. J.; Aktulga, H. M.; Verstraelen, T.; Grama, A.; van Duin, A. C. T. The ReaxFF reactive force-field: development, applications and future directions. *npj Computational Materials* **2016**, *2*.

(4) Islam, M. M.; Kolesov, G.; Verstraelen, T.; Kaxiras, E.; van Duin, A. C. T. eReaxFF: A Pseudoclassical Treatment of Explicit Electrons within Reactive Force Field Simulations. *Journal of Chemical Theory and Computation* **2016**, *12*, 3463–3472.

(5) Dittner, M.; Müller, J.; Aktulga, H. M.; Hartke, B. Efficient global optimization of reactive force-field parameters. *Journal of Computational Chemistry* **2015**, *36*, 1550–1561.

(6) van Duin, A. C. T.; Baas, J. M. A.; van de Graaf, B. Delft molecular mechanics: a new approach to hydrocarbon force fields. Inclusion of a geometry-dependent charge calculation. *Journal of the Chemical Society, Faraday Transactions* **1994**, *90*, 2881.

(7) Kaymak, M. C.; Rahnamoun, A.; O'Hearn, K. A.; van Duin, A. C. T.; Jr., K. M. M.; Aktulga, H. M. JAX-ReaxFF: A Gradient Based Framework for Extremely Fast Optimization of Reactive Force Fields. **2021**,

(8) Iype, E.; Hütter, M.; Jansen, A. P. J.; Nedea, S. V.; Rindt, C. C. M. Parameterization of a reactive force field using a Monte Carlo algorithm. *Journal of Computational Chemistry* **2013**, *34*, 1143–1154.

(9) Hubin, P. O.; Jacquemin, D.; Leherte, L.; Vercauteren, D. P. Parameterization of the ReaxFF reactive force field for a proline-catalyzed aldol reaction. *Journal of Computational Chemistry* **2016**, *37*, 2564–2572.

(10) Liu, H.; Wang, J.; Li, Q.; Haddad, A. M. Development of ReaxFF SFOH Force Field for SF 6 -H 2 O/O 2 Hybrid System Based on Synergetic Optimization by CMA-ES and MC Methodology. *ChemistrySelect* **2021**, *6*, 4622–4632.

(11) Pahari, P.; Chaturvedi, S. Determination of best-fit potential parameters for a reactive force field using a genetic algorithm. *Journal of Molecular Modeling* **2011**, *18*, 1049–1061.

(12) Larsson, H. R.; van Duin, A. C. T.; Hartke, B. Global optimization of parameters in the reactive force field ReaxFF for SiOH. *Journal of Computational Chemistry* **2013**, *34*, 2178–2189.

(13) Jaramillo-Botero, A.; Naserifar, S.; Goddard, W. A. General Multiobjective Force Field Optimization Framework, with Application to Reactive Force Fields for Silicon Carbide. *Journal of Chemical Theory and Computation* **2014**, *10*, 1426–1439.

(14) Yeon, J.; Chowdhury, S. C.; Daksha, C. M.; Gillespie, J. W. Development of Mg/Al/Si/O ReaxFF Parameters for Magnesium Aluminosilicate Glass Using an Artificial Neural Network-Assisted Genetic Algorithm. *The Journal of Physical Chemistry C* **2021**, *125*, 18380–18394.

(15) Trnka, T.; Tvaroška, I.; Koča, J. Automated Training of ReaxFF Reactive Force Fields for Energetics of Enzymatic Reactions. *Journal of Chemical Theory and Computation* **2017**, *14*, 291–302.

(16) Furman, D.; Carmeli, B.; Zeiri, Y.; Kosloff, R. Enhanced Particle Swarm Optimization Algorithm: Efficient Training of ReaxFF Reactive Force Fields. *Journal of Chemical Theory and Computation* **2018**, *14*, 3100–3112.

(17) Nakata, H.; Bai, S. Development of a new parameter optimization scheme for a reactive force field based on a machine learning approach. *Journal of Computational Chemistry* **2019**,

(18) Guo, F.; Wen, Y.-S.; Feng, S.-Q.; Li, X.-D.; Li, H.-S.; Cui, S.-X.; Zhang, Z.-R.; Hu, H.-Q.; Zhang, G.-Q.; Cheng, X.-L. Intelligent-ReaxFF: Evaluating the reactive force field parameters with machine learning. *Computational Materials Science* **2020**, *172*, 109393.

(19) Daksha, C. M.; Yeon, J.; Chowdhury, S. C.; Jr., J. W. G. Automated ReaxFF parametrization using machine learning. *Computational Materials Science* **2021**, *187*, 110107.

(20) Sengul, M. Y.; Song, Y.; Nayir, N.; Gao, Y.; Hung, Y.; Dasgupta, T.; van Duin, A. C. T. INDEEDopt: a deep learning-based ReaxFF parameterization framework. *npj Computational Materials* **2021**, *7*.

(21) Kennedy, J.; Eberhart, R. Particle swarm optimization. Proceedings of ICNN'95 - International Conference on Neural Networks. 1995; pp 1942–1948 vol.4.

(22) Storn, R.; Price, K. *Journal of Global Optimization* **1997**, *11*, 341–359.

(23) Cai, H.; Chung, C.; Wong, K. Application of Differential Evolution Algorithm for Transient Stability Constrained Optimal Power Flow. *IEEE Transactions on Power Systems* **2008**, *23*, 719–728.

(24) Wahab, M. N. A.; Nefti-Meziani, S.; Atyabi, A. A Comprehensive Review of Swarm Optimization Algorithms. *PLOS ONE* **2015**, *10*, e0122827.

(25) Luu, K.; Noble, M.; Gesret, A.; Belayouni, N.; Roux, P.-F. A parallel competitive Particle Swarm Optimization for non-linear first arrival traveltime tomography and uncertainty quantification. *Computers & Geosciences* **2018**, *113*, 81–93.

(26) Georgioudakis, M.; Plevris, V. A Comparative Study of Differential Evolution Variants in Constrained Structural Optimization. *Frontiers in Built Environment* **2020**, *6*.

(27) Igel, C.; Hansen, N.; Roth, S. Covariance Matrix Adaptation for Multi-objective Optimization. *Evolutionary Computation* **2007**, *15*, 1–28.

(28) Hansen, N.; Arnold, D. V.; Auger, A. *Springer Handbook of Computational Intelligence*; Springer Berlin Heidelberg, 2015; pp 871–898.

(29) Hansen, N. The CMA Evolution Strategy: A Tutorial. 2016.

(30) Akimoto, Y.; Auger, A.; Hansen, N. Comparison-based natural gradient optimization in high dimension. Proceedings of the 2014 Annual Conference on Genetic and Evolutionary Computation. 2014.

(31) Cui, Z. Alignment particle swarm optimization. 2009 8th IEEE International Conference on Cognitive Informatics. 2009.

(32) Shi, Y.; Eberhart, R. A modified particle swarm optimizer. 1998 IEEE International Conference on Evolutionary Computation Proceedings. IEEE World Congress on Computational Intelligence (Cat. No.98TH8360). 1998; pp 69–73.

(33) Eberhart, R.; Shi, Y. Comparing inertia weights and constriction factors in particle swarm optimization. Proceedings of the 2000 Congress on Evolutionary Computation. CEC00 (Cat. No.00TH8512). 2000; pp 84–88 vol.1.

(34) Wang, D.; Tan, D.; Liu, L. Particle swarm optimization algorithm: an overview. *Soft Computing* **2017**, *22*, 387–408.

(35) Clerc, M. The swarm and the queen: towards a deterministic and adaptive particle swarm optimization. Proceedings of the 1999 Congress on Evolutionary Computation-CEC99 (Cat. No. 99TH8406). 1999; pp 1951–1957 Vol. 3.

(36) Mussi, L.; Cagnoni, S.; Daolio, F. Empirical assessment of the effects of update synchronization in particle swarm optimization. Proceeding of the AIIA Workshop on Complexity, Evolution and Emergent Intelligence. 2009; pp 1–10.

(37) Rada-Vilela, J.; Zhang, M.; Seah, W. A performance study on synchronicity and neighborhood size in particle swarm optimization. *Soft Computing* **2013**, *17*, 1019–1030.

(38) Aziz, N. A. A.; Mubin, M.; Mohamad, M. S.; Aziz, K. A. A Synchronous-Asynchronous Particle Swarm Optimisation Algorithm. *The Scientific World Journal* **2014**, *2014*, 1–17.

(39) Carlisle, A.; Dozier, G. An off-the-shelf pso. in: Proceeding of Workshop on Particle Swarm Optimization. 2001.

(40) Xue, S.; Zhang, J.; Zeng, J. Parallel asynchronous control strategy for target search with swarm robots. *International Journal of Bio-Inspired Computation* **2009**, *1*, 151.

(41) Jiang, B.; Wang, N.; He, X. Asynchronous particle swarm optimizer with relearning strategy. IECON 2011 - 37th Annual Conference of the IEEE Industrial Electronics Society. 2011; pp 2341–2346.

(42) Schutte, J. F.; Reinbolt, J. A.; Fregly, B. J.; Haftka, R. T.; George, A. D. Parallel global optimization with the particle swarm algorithm. *International Journal for Numerical Methods in Engineering* **2004**, *61*, 2296–2315.

(43) Koh, B.-I.; George, A. D.; Haftka, R. T.; Fregly, B. J. Parallel asynchronous particle swarm optimization. *International Journal for Numerical Methods in Engineering* **2006**, *67*, 578–595.

(44) Rech, G. L.; Martinotto, A. L.; Balzaretti, N. M.; Perottoni, C. A. Fitting of interatomic potentials by a differential evolution algorithm. *Computational Materials Science* **2021**, *187*, 109929.

(45) Mezura-Montes, E.; Velázquez-Reyes, J.; Coello, C. A. C. A comparative study of

differential evolution variants for global optimization. Proceedings of the 8th annual conference on Genetic and evolutionary computation - GECCO '06. 2006.

(46) Das, S.; Suganthan, P. N. Differential Evolution: A Survey of the State-of-the-Art. *IEEE Transactions on Evolutionary Computation* **2011**, *15*, 4–31.

(47) Transition State Tools for VASP. `https://theory.cm.utexas.edu/vtsttools/`, Accessed: 2021-10-03.

(48) Rüger, R.; Franchini, M.; Trnka, T.; Yakovlev, A.; van Lenthe, E.; Philipsen, P.; van Vuren, T.; Klumpers, B.; Soini, T. ADF 2018, SCM, Theoretical Chemistry, Vrije Universiteit, Amsterdam, The Netherlands. `https://www.scm.com`.

(49) Henkelman, G.; Uberuaga, B. P.; Jónsson, H. A climbing image nudged elastic band method for finding saddle points and minimum energy paths. *The Journal of Chemical Physics* **2000**, *113*, 9901–9904.

(50) Henkelman, G.; Jónsson, H. Improved tangent estimate in the nudged elastic band method for finding minimum energy paths and saddle points. *The Journal of Chemical Physics* **2000**, *113*, 9978–9985.

(51) Sheppard, D.; Terrell, R.; Henkelman, G. Optimization methods for finding minimum energy paths. *The Journal of Chemical Physics* **2008**, *128*.

(52) Melander, M.; Laasonen, K.; Jónsson, H. Removing External Degrees of Freedom from Transition-State Search Methods using Quaternions. *Journal of Chemical Theory and Computation* **2015**, *11*, 1055–1062.

(53) Henkelman, G.; Jónsson, H. A dimer method for finding saddle points on high dimensional potential surfaces using only first derivatives. *The Journal of Chemical Physics* **1999**, *111*, 7010–7022.

(54) Heyden, A.; Bell, A. T.; Keil, F. J. Efficient methods for finding transition states in chemical reactions: Comparison of improved dimer method and partitioned rational function optimization method. *The Journal of Chemical Physics* **2005**, *123*, 224101.

(55) Kästner, J.; Sherwood, P. Superlinearly converging dimer method for transition state search. *The Journal of Chemical Physics* **2008**, *128*, 014106.

(56) Barkema, G. T.; Mousseau, N. Event-Based Relaxation of Continuous Disordered Systems. *Physical Review Letters* **1996**, *77*, 4358–4361.

(57) Olsen, R. A.; Kroes, G. J.; Henkelman, G.; Arnaldsson, A.; Jónsson, H. Comparison of methods for finding saddle points without knowledge of the final states. *The Journal of Chemical Physics* **2004**, *121*, 9776–9792.

(58) Bitzek, E.; Koskinen, P.; Gähler, F.; Moseler, M.; Gumbsch, P. Structural Relaxation Made Simple. *Physical Review Letters* **2006**, *97*, 170201.

(59) Hestenes, M.; Stiefel, E. Methods of conjugate gradients for solving linear systems. *Journal of Research of the National Bureau of Standards* **1952**, *49*, 409.

(60) Press, W. H.; Vetterling, W. T.; Teukolsky, S. A.; Flannery, B. P. *Numerical recipes*; Cambridge university press Cambridge, 1986; Vol. 818.

(61) Nocedal, J. Updating quasi-Newton matrices with limited storage. *Mathematics of Computation* **1980**, *35*, 773–773.

(62) Frederiksen, T.; Paulsson, M.; Brandbyge, M.; Jauho, A.-P. Inelastic transport theory from first principles: Methodology and application to nanoscale devices. *Phys. Rev. B* **2007**, *75*, 205413.

(63) Larsen, A. H. et al. The atomic simulation environment—a Python library for working with atoms. *Journal of Physics: Condensed Matter* **2017**, *29*, 273002.

(64) Sholl, D. S.; Steckel, J. A. *Density Functional Theory*; John Wiley & Sons, Inc., 2009.

(65) Frimannslund, L.; Steihaug, T. *Computer and Information Sciences II*; Springer London, 2011; pp 565–570.

(66) Jamil, M.; Yang, X.-S. A literature survey of benchmark functions for global optimisation problems. *International Journal of Mathematical Modelling and Numerical Optimisation* **2013**, *4*, 150–194, PMID: 55204.

(67) Ackley, D. H. *A Connectionist Machine for Genetic Hillclimbing*; Springer US, 1987.

(68) Bäck, T. *Evolutionary Algorithms in Theory and Practice: Evolution Strategies, Evolutionary Programming, Genetic Algorithms*; Oxford University Press: Oxford, New York, 1996.

(69) Qiang, J. I. A Unified Differential Evolution Algorithm for Global Optimization. **2014**,

(70) Törn, A.; Zilinskas, A. *Global Optimization*; Lecture Notes in Computer Science; Springer-Verlag: Berlin Heidelberg, 1989.

(71) Mühlenbein, H.; Schomisch, M.; Born, J. The parallel genetic algorithm as function optimizer. **1991**, *17*, 619–632.

(72) Rosenbrock, H. H. An Automatic Method for Finding the Greatest or Least Value of a Function. **1960**, *3*, 175–184.

(73) Picheny, V.; Wagner, T.; Ginsbourger, D. A benchmark of kriging-based infill criteria for noisy optimization. **2013**, *48*, 607–626.

(74) Lu, Y.-Z.; Chen, Y.-W.; Chen, M.-R.; Chen, P.; Zeng, G.-Q. *Extremal Optimization*; Auerbach Publications, 2018.

(75) Schwefel, H.-P. *Numerical optimization of computer models*; John Wiley & Sons, Inc., 1981.

(76) Yang, X.-S. Test Problems in Optimization. *X.-S. Yang, Test problems in optimization, in: Engineering Optimization: An Introduction with Metaheuristic Applications (Eds Xin-She Yang), John Wiley & Sons, (2010)* **2010**,

(77) Yang, X.-S. Firefly algorithm, stochastic test functions and design optimisation. *International Journal of Bio-Inspired Computation* **2010**, *2*, 78–84.

(78) Venter, G.; Sobieszczanski-Sobieski, J. Parallel Particle Swarm Optimization Algorithm Accelerated by Asynchronous Evaluations. **2006**, *3*, 123–137.

(79) Mueller, C. L.; Baumgartner, B.; Ofenbeck, G.; Schrader, B.; Sbalzarini, I. F. pCMALib. 2009.

(80) Zhabitskaya, E.; Zhabitsky, M. *Asynchronous Differential Evolution*; Springer Berlin Heidelberg, 2012; pp 328–333.

(81) Sudholt, D. *Parallel Evolutionary Algorithms*; Springer Berlin Heidelberg, 2015; pp 929–959.

(82) Stottmeister, D.; Groß, A. Strain Dependence of Metal Anode Surface Properties. **2020**, *13*, 3147–3153.

(83) Burton, W. K.; Cabrera, N.; Frank, F. C. The Growth of Crystals and the Equilibrium Structure of their Surfaces. *Philosophical Transactions of the Royal Society A: Mathematical, Physical and Engineering Sciences* **1951**, *243*, 299–358.

(84) Luu, K. Stochopy. `https://github.com/keurfonluu/stochopy`, 2021; `https://github.com/keurfonluu/stochopy`.

(85) Gaissmaier, D.; Fantauzzi, D.; Jacob, T. First principles studies of self-diffusion processes on metallic lithium surfaces. *The Journal of Chemical Physics* **2019**, *150*, 041723.

(86) Gaissmaier, D.; Borg, M. v. d.; Fantauzzi, D.; Jacob, T. Microscopic Properties of Na and Li—A First Principle Study of Metal Battery Anode Materials. *ChemSusChem* **2020**, *13*, 771–783.

(87) Kresse, G.; Furthmüller, J. Efficient iterative schemes for *ab initio* total-energy calculations using a plane-wave basis set. *Physical Review B* **1996**, *54*, 11169–11186.

(88) Kresse, G.; Furthmüller, J. Efficiency of ab-initio total energy calculations for metals and semiconductors using a plane-wave basis set. *Computational Materials Science* **1996**, *6*, 15 – 50.

(89) Blöchl, P. E. Projector augmented-wave method. *Physical Review B* **1994**, *50*, 17953–17979.

(90) Kresse, G.; Joubert, D. From ultrasoft pseudopotentials to the projector augmented-wave method. *Physical Review B* **1999**, *59*, 1758–1775.

(91) Perdew, J. P.; Burke, K.; Ernzerhof, M. Generalized Gradient Approximation Made Simple. *Physical Review Letters* **1996**, *77*, 3865–3868.

(92) Wellendorff, J.; Lundgaard, K. T.; Møgelhøj, A.; Petzold, V.; d. Landis, D.; Nørskov, J. K.; Bligaard, T.; Jacobsen, K. W. Density functionals for surface science: Exchange-correlation model development with Bayesian error estimation. *Physical Review B* **2012**, *85*, 316.

(93) Monkhorst, H. J.; Pack, J. D. Special points for Brillouin-zone integrations. *Physical Review B* **1976**, *13*, 5188–5192.

(94) van Duin, A. C. T.; Goddard, W. A.; Islam, M. M.; van Schoot, H.; Trnka, T.; Yakovlev, A. L. ReaxFF 2021.1, SCM, Theoretical Chemistry, Vrije Universiteit, Amsterdam, The Netherlands. `https://www.scm.com`.

(95) Verstraelen, T.; Ayers, P. W.; Speybroeck, V. V.; Waroquier, M. ACKS2: Atom-condensed Kohn-Sham DFT approximated to second order. **2013**, *138*, 074108.

(96) Islam, M. M.; Ostadhossein, A.; Borodin, O.; Yeates, A. T.; Tipton, W. W.; Hennig, R. G.; Kumar, N.; van Duin, A. C. T. ReaxFF molecular dynamics simulations on lithiated sulfur cathode materials. *Phys. Chem. Chem. Phys.* **2015**, *17*, 3383–3393.

(97) Ostadhossein, A.; Kim, S.-Y.; Cubuk, E. D.; Qi, Y.; van Duin, A. C. T. Atomic Insight into the Lithium Storage and Diffusion Mechanism of SiO2/Al2O3 Electrodes of Lithium Ion Batteries: ReaxFF Reactive Force Field Modeling. **2016**, *120*, 2114–2127.

(98) Raju, M.; Ganesh, P.; Kent, P. R. C.; van Duin, A. C. T. Reactive Force Field Study of Li/C Systems for Electrical Energy Storage. **2015**, *11*, 2156–2166.

(99) Csonka, G. I.; Perdew, J. P.; Ruzsinszky, A.; Philipsen, P. H. T.; Lebègue, S.; Paier, J.; Vydrov, O. A.; Ángyán, J. G. Assessing the performance of recent density functionals for bulk solids. *Physical Review B* **2009**, *79*, 354.

(100) Alchagirov, A. B.; Perdew, J. P.; Boettger, J. C.; Albers, R. C.; Fiolhais, C. Energy and pressure versus volume: Equations of state motivated by the stabilized jellium model. *Physical Review B* **2001**, *63*, 29.

(101) Alchagirov, A. B.; Perdew, J. P.; Boettger, J. C.; Albers, R. C.; Fiolhais, C. Reply to "Comment on 'Energy and pressure versus volume: Equations of state motivated by the stabilized jellium model' ". *Physical Review B* **2003**, *67*.

(102) Groß, A. *Theoretical Surface Science*; Springer Berlin Heidelberg, 2009.

(103) Tyson, W.; Miller, W. Surface free energies of solid metals: Estimation from liquid surface tension measurements. *Surface Science* **1977**, *62*, 267–276.

(104) Vitos, L.; Ruban, A.; Skriver, H.; Kollár, J. The surface energy of metals. *Surface Science* **1998**, *411*, 186–202.

(105) Ding, F.; Xu, W.; Graff, G. L.; Zhang, J.; Sushko, M. L.; Chen, X.; Shao, Y.; Engelhard, M. H.; Nie, Z.; Xiao, J.; Liu, X.; Sushko, P. V.; Liu, J.; Zhang, J.-G. Dendrite-Free Lithium Deposition via Self-Healing Electrostatic Shield Mechanism. *Journal of the American Chemical Society* **2013**, *135*, 4450–4456.

(106) Zhang, Y.; Qian, J.; Xu, W.; Russell, S. M.; Chen, X.; Nasybulin, E.; Bhattacharya, P.; Engelhard, M. H.; Mei, D.; Cao, R.; Ding, F.; Cresce, A. V.; Xu, K.; Zhang, J.-G. Dendrite-Free Lithium Deposition with Self-Aligned Nanorod Structure. **2014**, *14*, 6889–6896.

(107) ling Ma, J.; lu Meng, F.; Yu, Y.; peng Liu, D.; min Yan, J.; Zhang, Y.; bo Zhang, X.; Jiang, Q. Prevention of dendrite growth and volume expansion to give high-performance aprotic bimetallic Li-Na alloy–O2 batteries. **2018**, *11*, 64–70.

(108) Liu, H.; Cheng, X.-B.; Huang, J.-Q.; Kaskel, S.; Chou, S.; Park, H. S.; Zhang, Q. Alloy Anodes for Rechargeable Alkali-Metal Batteries: Progress and Challenge. **2019**, *1*, 217–229.

(109) Bale, C. W. The Li-Na (Lithium-Sodium) system. **1989**, *10*, 265–268.

(110) Senftle, T. P.; Meyer, R. J.; Janik, M. J.; van Duin, A. C. T. Development of a ReaxFF potential for Pd/O and application to palladium oxide formation. *The Journal of Chemical Physics* **2013**, *139*, 044109.

(111) Senftle, T. P.; van Duin, A. C.; Janik, M. J. Determining in situ phases of a nanoparticle catalyst via grand canonical Monte Carlo simulations with the ReaxFF potential. *Catalysis Communications* **2014**, *52*, 72–77.

(112) Lippmann, G., et al. Relations entre les phénomènes électriques et capillaires. Ph.D. thesis, Gauthier-Villars Paris, France, 1875.

(113) Hagopian, A.; Doublet, M.-L.; Filhol, J.-S. Thermodynamic origin of dendrite growth in metal anode batteries. *Energy & Environmental Science* **2020**, *13*, 5186–5197.

(114) Reuter, K.; Scheffler, M. First-principles kinetic Monte Carlo simulations for heterogeneous catalysis: Application to the CO oxidation atRuO2(110). **2006**, *73*, 045433.

(115) Jansen, A. P. J. *An Introduction to Kinetic Monte Carlo Simulations of Surface Reactions*; Springer Berlin Heidelberg, 2012.

(116) Trygubenko, S. A.; Wales, D. J. A doubly nudged elastic band method for finding transition states. *The Journal of Chemical Physics* **2004**, *120*, 2082–2094.

(117) O'Hearn, K. A.; Swift, M. W.; Liu, J.; Magoulas, I.; Piecuch, P.; van Duin, A. C. T.; Aktulga, H. M.; Qi, Y. Optimization of the Reax force field for the lithium–oxygen system using a high fidelity charge model. **2020**, *153*, 084107.

(118) Ojwang, J. G. O.; van Santen, R.; Kramer, G. J.; van Duin, A. C. T.; Goddard, W. A. Modeling the sorption dynamics of NaH using a reactive force field. **2008**, *128*, 164714.

(119) Hjertenæs, E.; Nguyen, A. Q.; Koch, H. A ReaxFF force field for sodium intrusion in graphitic cathodes. **2016**, *18*, 31431–31440.

(120) Hahn, S. H.; Rimsza, J.; Criscenti, L.; Sun, W.; Deng, L.; Du, J.; Liang, T.; Sinnott, S. B.; van Duin, A. C. T. Development of a ReaxFF Reactive Force Field for NaSiOx/Water Systems and Its Application to Sodium and Proton Self-Diffusion. **2018**, *122*, 19613–19624.